

**SATELLITE APPLICATION FACILITY ON SUPPORT TO
OPERATIONAL HYDROLOGY AND WATER MANAGEMENT
(H-SAF)**

**VISITING SCIENTIST ACTIVITY IN SUPPORT OF WP 2400
VS PROGRAMME**

ACTIVITY REPORT

**Enhancement of H-SAF Precipitation Retrieval Algorithm/Product over Mountainous
Regions**

Ahmet ÖZTOPAL

Istanbul Technical University (ITU)
Meteorological Department
Istanbul, Turkey

Alberto MUGNAI, Daniele CASELLA, Marco FORMENTON, Paolo SANÒ

Istituto di Scienze dell'Atmosfera e del Clima (ISAC)
Consiglio Nazionale delle Ricerche (CNR)
Roma, Italy

İbrahim SÖNMEZ

Turkish Meteorological Service (TMS)
Remote Sensing Division
Ankara, Turkey

Zekai ŞEN

Istanbul Technical University (ITU)
Hydraulic Division
Istanbul, Turkey

PREFACE

Turkey is a mountainous country which includes 4 different climate structure and due to these special features, an enhanced Bayesian Algorithm is employed in the processing schedule of the project. This algorithm is developed based on Cloud-Radiation Database (CDR) from 14 rainy cases by Dr. Alberto MUGNAI and his team (Dr. Daniele CASELLA, Dr. Marco FORMENTON and Dr. Paolo SANÒ) from the Institute of Atmospheric Sciences and Climate (ISAC) of the Italian National Research Council (CNR) work in EUMETSAT - Application Facility on Support to Operational Hydrology and Water Management (HSAF). Besides, Dr. İbrahim SÖNMEZ and Dr. Zekai ŞEN assisted in radar and raingauge data collection, assessment and validation. I would like to thank you all for your valuable assistances, without which this report could not be completed successfully.

Moreover, I would also like to thank Dr. Sante LAVIOLA, Dr. Vincenzo LEVIZZANI and Dr. Francesco Di PAOLA for their contributions.

Dr. Ahmet ÖZTOPAL

1. INTRODUCTION

It is rather a very difficult task to determine ground rainfall amounts from few SSMI/S channels. Although ground rainfall cannot be observed from the space directly, but knowledge about the cloud physics helps to estimate the amount of ground rainfall. SSMI/S includes so much information about the atmospheric structure, however it cannot provide cloud micro-physical structural information. In such a situation, in the rainfall algorithm, besides the SSMI/S data, it is necessary to incorporate cloud micro-physical properties from an external data source. These properties can be obtained quite simply by the help of Cloud Resolving Model (CRM). Later, in addition to all available data, also micro-physical properties obtained from Radiative Transfer Model (RTM) help to determine the SSMI/S brightness temperatures (Brightness temperatures – TBs), which can then be correlated with Cloud-Radiation Database (CRD) data generation (Mugnai, et al., 2009).

SSMI/S satellite data and CDR provide a common basis for rainfall prediction procedure through CDR Bayesian probability algorithm, which combines the two sets of data in a scientific manner. The first applications of this algorithm, which is being used up today, is due to various researchers (Mugnai et al., 2001; Di Michele et al., 2003, 2005; Tassa et al., 2003, 2006)

In this work, in order to establish a reflection of available data processing CDR CRM University of Wisconsin – Non-hydrostatic Modeling System (UW-NMS) model is employed, which is first developed by Prof. Gregory J. Tripoli (Tripoli, 1992; Tripoli and Smith, 2008). It is also used by Turkish Meteorological Service by benefiting from radar network data, and finally 14 simulations are realized in this study.

2. STRUCTURE OF CLIMATE IN TURKEY

Turkey is a mountainous country located between warm and sub-tropical climate regions. Even though three sides are surrounded by seas. Mountain chain extensions and morphology of Turkey, naturally, lead to various climate types within the country. Along the coastal regions due to maritime effects warm climate types prevail, whereas continental climate type exists in the central regions, because of the Taurus and Northern Anatolian Mountains extensions as barrier from the coastal areas. According to Atalay (1997) and the universal climate classification, the following climate types prevail in Turkey. These climate regions are shown in Figure 2.1.

1) Continental climate (a, b, c and d): Temperature differences between winter and summer seasons is rather high; precipitation takes place frequently in winter and spring seasons and during summer dry spells occur. Depending on the precipitation and temperature features continental climate has four versions.

2) Mediterranean Climate: Summers are hot and dry but in winters warm with heavy precipitation exists. Hail and snow fall events are scarce along the coastal regions. However, at high elevations winters are snowy and cold.

3) Marmara Climate: During winter, it is as hot as Mediterranean climate, but in summer not very rainy as much as Black Sea region. Winters are cold as continental

climate and summers are hot and dry. Due to these features, Marmara climate has its position between continental Black Sea and Mediterranean Sea climates, as a transitional zone.

4) Black Sea Climate: Temperature differences between summer and winter are not very significant. Summers are rather cool, winters at coastal areas are warm but with snow and cold air at high elevation areas. Each season is rainy, and hence, there is not water scarcity or stress.

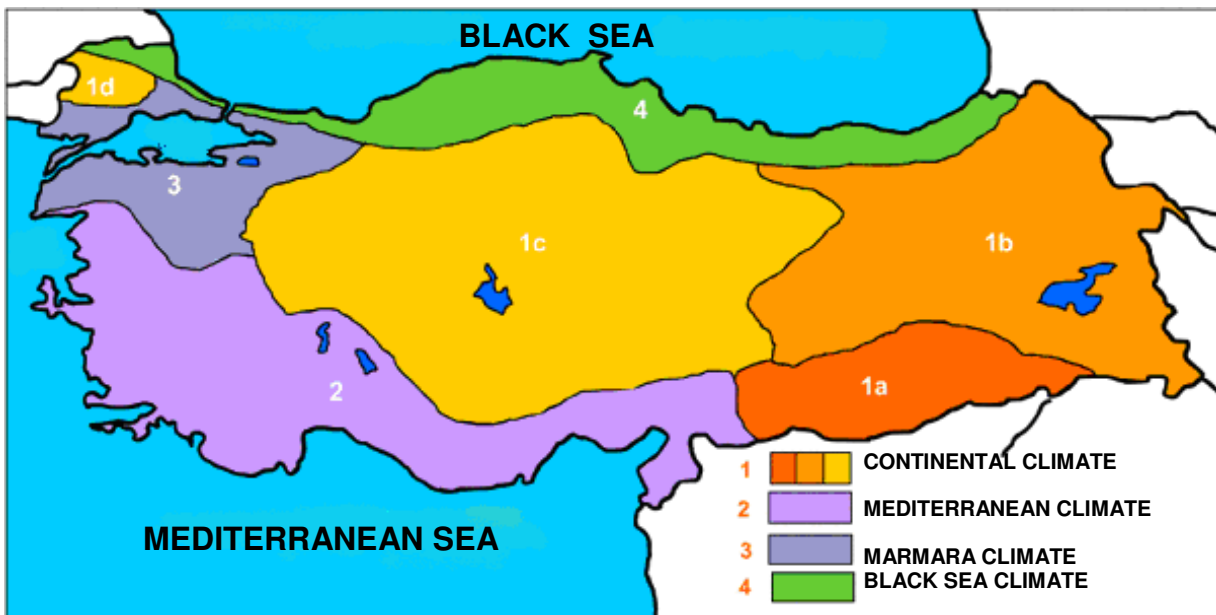


Figure 2.1. Climate regions in Turkey

3. OBSERVATION NETWORK IN TURKEY

As it is obvious in Figure 3.1, there are about 206 automatic stations in the western part of the country and they are within an the same observation network. The time resolution of precipitation records at these station is almost 1 minute.



Figure 3.1. Automated Weather Observation System (AWOS) station distribution in Turkey

In total, there are four C Band Doppler radars and one of them has dual polarization property (Figure 3.2). Among these, only İstanbul (a) and Balıkesir (b) located location radars are adopted for in this study, but unfortunately, these they do not have dual polarization property. In this work ,CAPPI product was used for radar data.

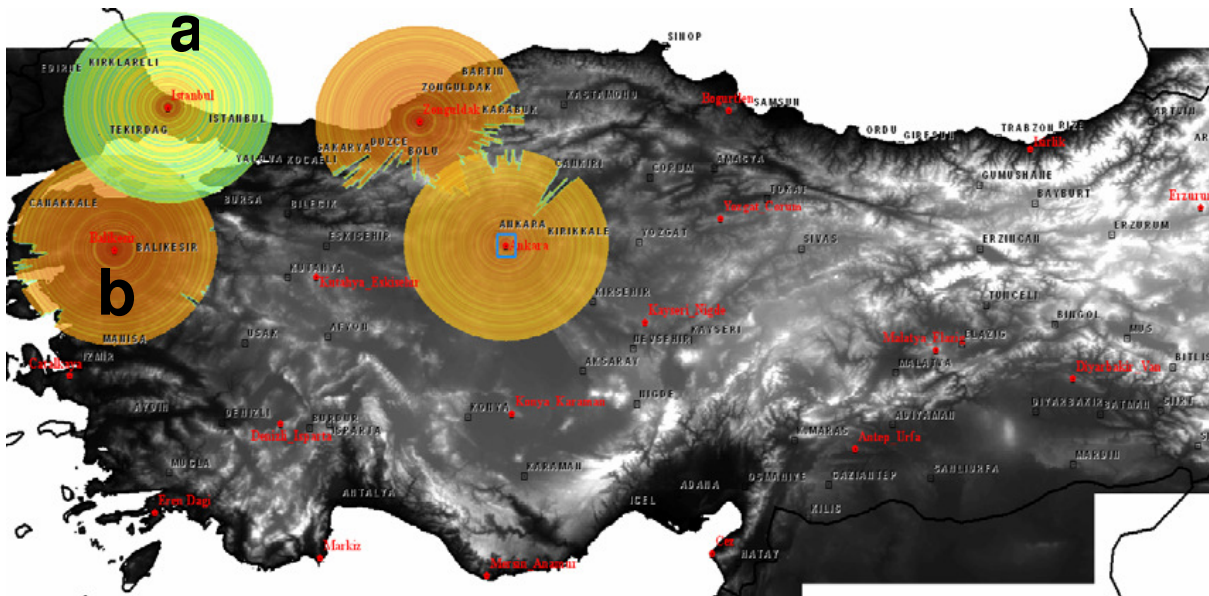


Figure 3.2. Radars and their coverage area in Turkey.

4. METHODOLOGY

4.1. Description of the Models

4.1.1. Cloud Resolving Model (CRM)

Time-dependent cloud/mesoscale numerical model with the three-dimensional (3-D) UW-NMS, is capable of simulating atmospheric phenomena with horizontal scales ranging from the microscale (turbulence) to the synoptic scale (extratropical cyclones, fronts, etc.). The non-Boussinesq quasi-compressible dynamical equations provide the basis on a set of assumptions as the model thermodynamics are based on the prediction of a moist ice-liquid entropy variable, designed to be conservative over all ice and liquid adiabatic process (Tripoli and Cotton, 1981). Vorticity, kinetic energy and potential entrophy, which are among the dynamic properties of flow are conserved by the advection scheme in the aforementioned model, which employs variable step topography. This approach is capable of capturing steep topographical slopes, and accurately represents subtle topographic variations. Additionally, classical conservation equations are used for the specific humidity of total water and several ice and liquid water hydrometeor categories. A two-way multiply nested Arakawa “C” grid system modeling is the basis of the approach in this report, and it cast on a rotated spherical grid system, which includes multiple 2-way nesting capability. Such an approach helps to adjust locally enhanced resolutions in the most convenient way.

The new version of UW-NMS includes microphysical module within H-SAF, which is a modified form of the scheme (Flatau et al., 1989; Cotton et al., 1986). Furthermore, the

ice categories treatment and the precipitation physical specifications are different from the original in the sense of performance enhancement. There are 6 hydrometeor categories as follows:

- 1) Suspended cloud droplets,
- 2) Precipitating rain drops,
- 3) Suspended pristine ice crystals, and precipitation,
- 4) Ice aggregates,
- 5) Low-density graupel particles (or snow) and,
- 6) High density graupel particles.

In the application procedure, within the same grid volume at any given few or all these categories may be used (for instance a couple of frozen and liquid hydrometeors) for the hydrometeor category interaction.

4.1.2. Radiative Transfer Model (RTM)

It is necessary to include upwelling brightness temperatures (TBs) for simulation purposes with the expectation of a radiative transfer (RT) code application to the simulated precipitation events' microphysical outputs, which lead to the upwelling radiances computation based on the satellite footprints' simulation. Such approaches cause heavy computation overburden, because they are dependent on the cloud model simulation of the macrophysical structure. It is, therefore, for practical purposes, better to use simpler models in one dimension, and hence, they are faster but have less accuracy. However, in this study a 3-D adjusted plane parallel RT scheme is adopted as developed by Roberti et al. (1994) (see also Liu et al., 1996; Bauer et al., 1998; Tassa et al., 2003). The cloud model paths along the radiometer direction of sight help to generate the plane-parallel cloud structures rather than from the vertical cloud model columns. The RT approach along a slanted profile in the direction of observation of the radiometer is employed with confidence. One can observe that the downward flux is computed through the cloud structure along the specular line that is reflected at the surface. It is observed that the used method is computationally convenient and efficient. It also accounts for the geometrical and partially reducing errors in radiative transfer modelling. A genuine 3-D radiative effects are not taken into consideration, due to the fact that the radiation is still trapped inside the slanted (and reflected) column. If there are enhanced horizontal inhomogeneities, then the same approach may produce significant discrepancies with a fully 3D model outputs. Roberti et al., (1994) and Bauer et al., (1998) studied the performances of the slanted-path plane-parallel RT approximation and they agree on the error limitations concerning a few K on average scenes, Local values may be important in case of large horizontal gradients such as at the cloud edges (Liu et al., 1996; Czekala et al., 2000; Olson et al., 2001).

After the completion of the monochromatic upwelling radiances at high resolution (i.e., at the resolution of the CRM model – 2 km) then the upwelling TBs at sensor resolution is computed for each channel through instrument transfer function. This is equivalent to the first integrating the monochromatic upwelling radiances over the channel-width. It takes into account the channel spectral responsivity, and integrates the channel upwelling radiances over the field of view (i.e., over all cloud-model pixels that are contained in the field of view) Finally, it also takes into account the radiometer antenna pattern and radiometric noise. Subsequently, the high-resolution hydrometeor liquid/ice water content and the corresponding precipitation rate profiles for rain and ice are extracted from the cloud model simulations. They are then averaged over the field of view in order to produce almost the same quantities at sensor resolution. The cloud structure definition is very important because it is associated with the simulated TBs. In general, each

channel has a different cloud structure. It fills up the slanted elliptical cylinder with comparable sizes to the cross-track and along-track resolutions and it should be associated with each TB point of the database. Such a strategy helps to make the multi-frequency retrieval rather complex and not univocal. It is, therefore, very convenient to choose a common single resolution for the microphysical parameters that belong to the cloud-radiation database.

CRM simulations outputs provide inputs for the radiative transfer model (RTM) for upwelling TBs generations, which are the vertical profiles of the liquid/ice water contents (LWC and IWC, respectively) of the various hydrometeors. Of course, they are also coupled with the surface temperature and the temperature/moisture profiles. Additional outputs are radiometer model, the surface emissivity model, and the single-scattering model.

Radiometer Model Structure

It provides a secondary input to the RT model. It also specifies all characteristics of the radiometer for simulation. Among the variables are the frequency, polarization and width of the candidate channels, view angle of the radiometer; field of view and antenna pattern of the various channels. Instrument Transfer Function should be defined for each channel for the upwelling TBs computations from the upwelling monochromatic radiances. In this assessment, the following channel characteristics are important concerning the conically-scanning radiometers.

- 1) Special Sensor Microwave Imager (SSM/I)
- 2) Special Sensor Microwave Imager (SSMIS)
- 3) TRMM Microwave Imager (TMI), and,
- 4) Advanced Microwave Scanning Radiometer-EOS (AMSR-E)

Surface Emissivity Models

Surface emissivity impacts show themselves in the upwelling TBs more frequently at the lower frequencies as dependents on the frequency and polarization, observation geometry, and surface characteristics (land/ocean, surface roughness, type of soil and soil cover, soil humidity, etc.). Three different surface emissivity models are selected for the purpose of representing the different surface backgrounds of the selected CRM simulations in the best possible manner. These surface emissivity models are as follows.

- 1) The forest and agricultural land surface emissivity for land surfaces (Hewison, 2001),
- 2) The fast and accurate ocean emissivity model for a sea surface, (English and Hewison, 1998; Hewison and English, 2000 and Schluessel et al, 1998). They provide accurate surface emissivity estimations between 10 and 200 GHz for view angles up to 60° and wind speeds from 0 to 20 m/s,
- 3) The snow emissivity model that has been empirically derived for snow covered *surfaces* from satellite retrievals and ground-based measurements (Hewison, 1999). Five different snow cover types are considered for full range of snow emissivity. Such studies are presented by some studies in the literature, such as the forest +snow, deep dry snow, fresh wet snow, frozen soil, first year ice, compact snow.

Single-Scattering Models

It is a direct way to compute the single-scattering properties of the various hydrometeor species in the cases of pure water and ice spheres only such as the Mie scattering. However, it can be a major challenge for natural ice hydrometeors due to their

wide variety of sizes, densities, and shapes. Information on shape is not available from the UW-NMS microphysical parameterization scheme, and therefore, for a successful study it is necessary to depend on a set of assumptions as follows.

1) *Liquid* (cloud and rain) particles have spherical forms, which are homogeneous, and accordingly their scattering properties can be computed by Mie theory (Bohren and Huffman, 1983). This approach necessitates the use of an efficient code as developed by Wiscombe (1980).

2) *Graupel* particles are in the form of spheres with densities almost equal to pure ice (0.9 g cm⁻³) with “equivalent homogeneous spheres” and an effective dielectric procedure combining the dielectric functions of ice and air (or water, in case of melting). In this it is carried out according to the effective medium Maxwell-Garnett mixing theory for a two-component mixture of inclusions of air (water) in an ice matrix (Bohren and Huffman, 1983).

3) *Pristine ice particles* are highly non-spherical, and hence it is convenient to use the Grenfell and Warren (1999) approximations (also Neshyba et al., 2003). The single-scattering properties of each nonspherical ice particle are computed by means of a collection of n_s equal-size solid-ice spheres with a diameter, that is determined by the volume, V , to cross-sectional area, A , ratio as V/A all of the original nonspherical ice particle. The UW-NMS simulation outputs yield the volume values. On the other hand, the cross-sectional area comes through the observational relationship as $A/(\pi D^2/4) = C_0$. For several different individual particle habits D (in cm) is the maximum diameter of the particle, while the coefficients C_0 and C (in appropriate cgs units) depend on ice particle habit (Heymsfield and Miloshevich, 2003). For pristine ice crystals, $C_0 = 0.18$ and $C = 0.2707$, that are indicated by the same authors as appropriate averages for midlatitude, continental mixed-habit cirrus clouds. It is possible to obtain the diameter, D_s , and the number, n_s , by the following formulations.

$$D_s = \frac{\rho}{\rho_{ice}} \frac{D}{C_0 D^C} \quad n_s = \frac{C_0}{1-C} \frac{D^{3+C}}{D_s^3}$$

where, $\rho_{ice} = 0.916 \text{ g cm}^{-3}$ while the density ρ of the pristine ice crystals is usually equal to 0.1 g cm^{-3} .

It is well known that the snowflakes and ice aggregates have low-densities. Additionally, fluffy ice particles (as long as they are completely frozen) cannot be modelled according to Maxwell-Garnett mixing theory because “equivalent homogeneous soft-ice spheres” would have, according to Mie theory, very large asymmetry factors (> 0.9) at the higher microwave frequencies. Hence, it would not be adequately “cool” for the upwelling radiation. In order to overcome this problem, one can use the Surussavadee (2006) model where non-spherical scattering results are fitted for spheres by Mie theory and calculations with a density that is a function of the wavelength.

4.2. Generation of the CRD Databases

14 precipitation cases, which were observed between 2007 – 2009, are selected for making CDR database (Table 4.1). These simulations are realized for red boxes in Figure 4.1.

Table 4.1: Details of the 14 NMS simulations

START UP (spin off)		CASE STUDY		SIMULATION DURATION		
Date	hour	DATE	hour (start)	HOURS	Lat	Lon (E > 0)
2007/08/26	12.00	2007/08/27	00.00	60	40.28	32.64
2007/10/12	12.00	2007/10/13	00.00	60	40.13	28.27
2007/10/12	12.00	2007/10/13	00.00	60	40.28	32.64
2007/10/22	12.00	2007/10/23	00.00	60	40.13	28.27
2007/10/22	12.00	2007/10/23	00.00	60	40.28	32.64
2008/03/19	06.00	2008/03/19	18.00	60	40.13	28.27
2008/09/16	12.00	2008/09/17	00.00	60	40.28	32.64
2008/10/02	12.00	2008/10/03	00.00	60	40.15	28.28
2008/10/25	12.00	2008/10/26	00.00	60	40.13	28.28
2008/12/17	12.00	2008/12/18	00.00	60	40.13	28.27
2009/01/03	12.00	2009/01/04	00.00	60	40.15	28.28
2009/02/07	12.00	2009/02/08	00.00	60	40.15	28.28
2009/04/21	12.00	2009/04/22	00.00	48	40.15	28.28
2009/05/17	18.00	2009/05/18	06.00	54	40.15	28.28

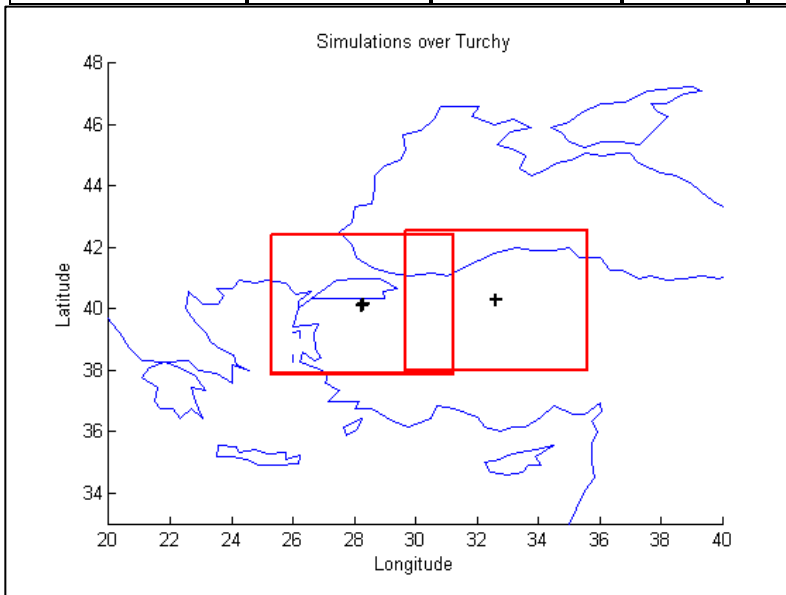


Figure 4.1. Red boxes show the inner domains of UW-NMS simulations

In this work, three nested, concentric and steady grids were used for each simulation. UW-NMS is non-hydrostatic and has 3 nested domain (Table 4.2). Domain 1, which is first and outer grid, was set at 50 km resolution and has 92 grid points. For domain 2, there are 92 grid points and resolution is 10 km. The third and inner grid, which was set up at 2 km, has 252 grid points. Moreover, 35 vertical levels were valid for all grids and maximum height was set at 18 km.

In figure 4.2 and 4.3, examples of UW-NMS rainfall and total water (ice + liquid) can be seen.

Table 4.2. NMS model features

Non-hydrostatic

Three nested domains:

- Domain 1, 50 Km resolution with 92 grid points
- Domain 2, 10 Km resolution with 92 grid points
- Domain 3, 2 Km resolution with 252 grid points

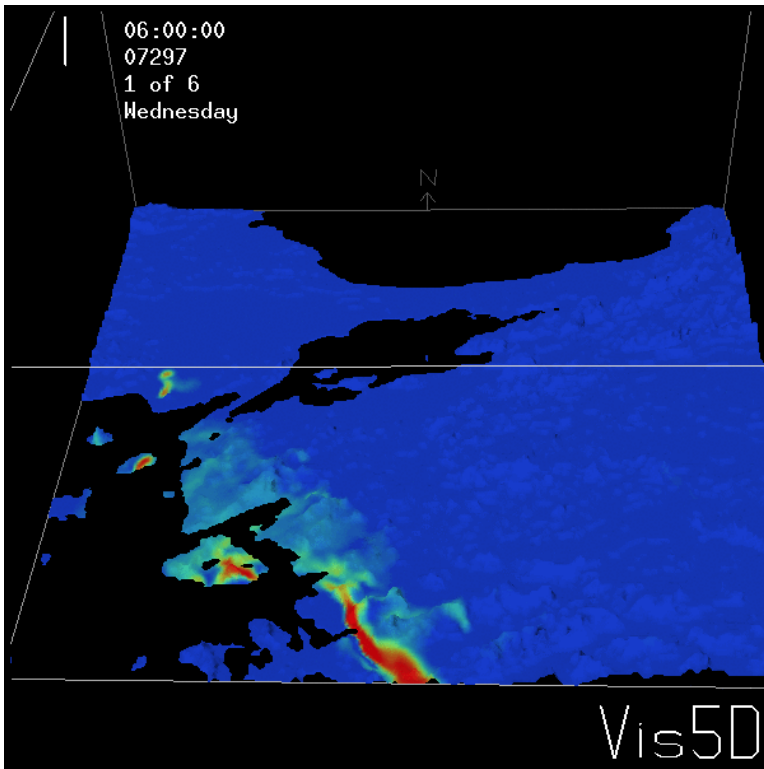


Figure 4.2. Example of UW-NMS model rainfall rate in Domain 3.

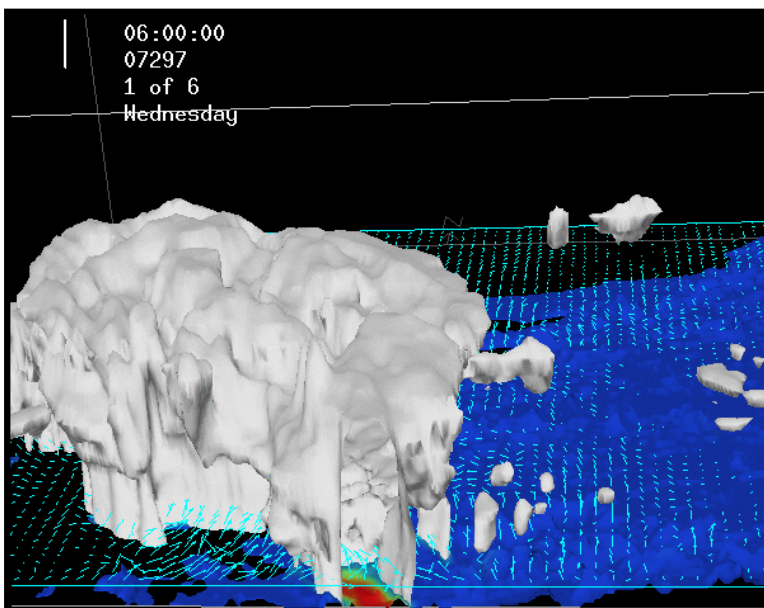


Figure 4.3. Example of UW-NMS total water (ice+liquid) in Domain 3.

4.3. The CDRD Retrieval Algorithm

Especially, Bayesian methodology helps to retrieve the precipitation indicators from satellite-borne microwave radiometers coupled with the Cloud Radiation Databases (CRDs) and they are composed of thousands of detailed microphysical cloud profiles. These are taken from Cloud Resolving Model (CRM) simulations, including the corresponding brightness temperatures (TBs), which is calculated by applying radiative transfer schemes to the CRM outputs. CRD's play the role of generator for the CRM simulations of past precipitation events. Subsequently, they can be used for the analysis of new events' satellite observations.

Figure 4.4 indicates the block diagram of our CDRD Bayesian algorithm, where the following significant points must be taken into consideration for relevant interpretations (Sanò et al,2010).

1) Prior to the estimation of TB measurements it is necessary to process the TBs measured by SSM/I or SSMIS (data processing block). This has to be done for each channel at the same geographical latitude and longitude position, Such interpolation procedures are helpful for the low resolution channels.

2) A "screening procedure" is employed for the data analysis for the decision whether to reject areas (pixels) either having incorrect TB values due to sensor errors or recognized as areas without rain or with a very low probability of rain.

3) The pixel selection is achieved by inversion algorithm, which uses a Bayesian distance concept between the measured multi-frequency TB vector and all simulated multi-frequency TB vectors of the CDRD database.

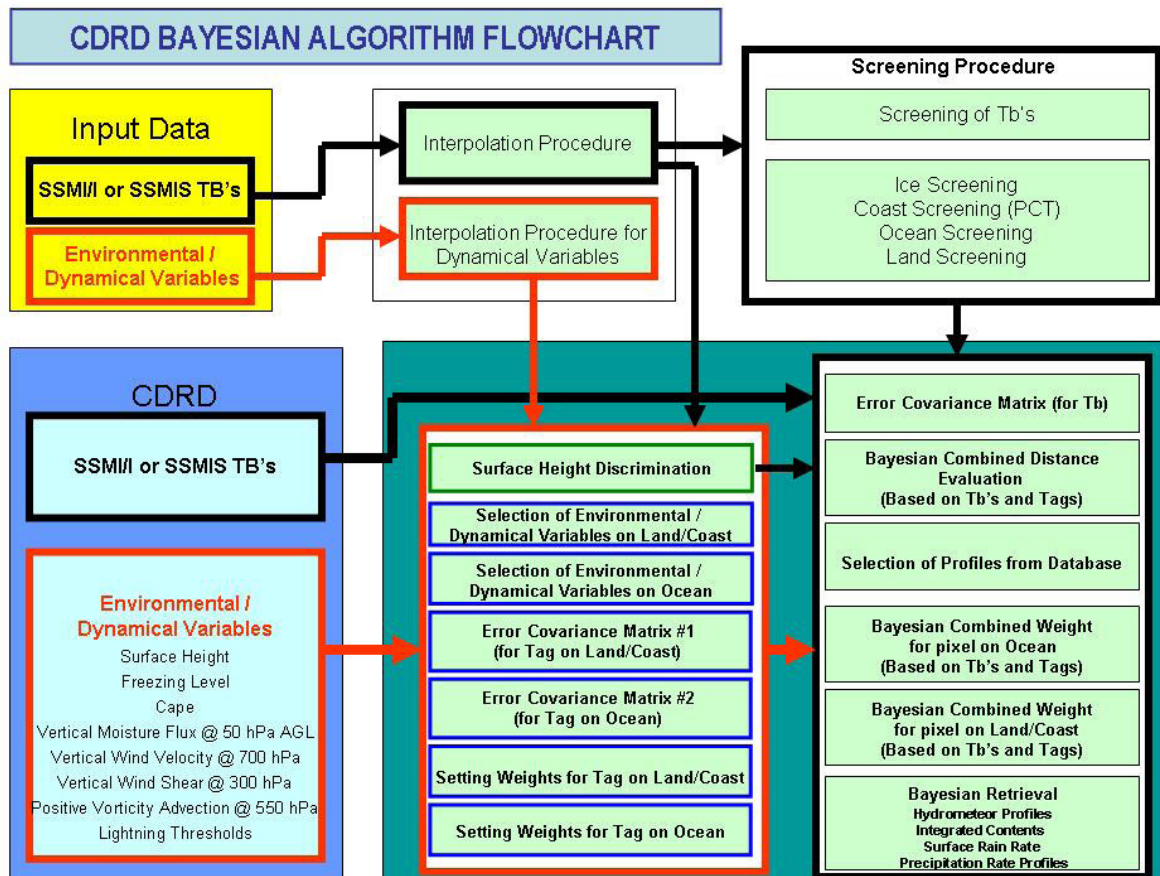


Figure 4.4. Block diagram of the CDRD Bayesian algorithm.

5. ANALYSIS PROCEDURE

5.1. Statistics

There are 14 NMS simulations at high-resolution (2 km) profiles, which are associated with TBs as averages to produce the sensor-resolution (15 km) profiles and the corresponding TBs (SSM/I – SSMIS observation simulators). Table 5.1 includes the components of each profile in the CRD database for SSM/I.

Table 5.1. CRD database for SSM/I components of each profile

TB19.35V (K)	TB37.00H (K)
TB19.35H (K)	TB85.00V (K)
TB22.24V (K)	TB85.00H(K)
TB37.00V (K)	
Vert-integrated cloud water path (kg/m**2)	
Vert-integrated rain water path (kg/m**2)	
vert-integrated graupel water path (kg/m**2)	
vert-integrated pristine water path (kg/m**2)	
vert-integrated snow water path (kg/m**2)	
vert-integrated aggregates water path (kg/m**2)	
Surface rain rate (mm/hr)	
Surface pristine (mm/hr)	
Surface aggregate (mm/hr)	
Surface graupel (mm/hr)	
Surface snow (mm/hr)	
Profile number	Latitude Longitude
Percent land	Percent snow Percent
ice	
Height of surface (km)	
Iztop	

5.1.1. Microphysical Quantities

Some simple but significant statistics of the cloud structure microphysical properties are presented in Table 5.2. Additionally, Figures 5.1 and 5.2 give the CRD Turkish database. It is possible to sense that low water/ice contents and low precipitation are in the majority with a large variability in the cloud microphysical properties, which can be related to the coverage of different climatic regions, where types of precipitation and seasonal variations occur in Turkey.

Table 5.2. Statistics indexes of simulated TBs over land.

	Mean	Variance	Spread
Cloud Columnar Content (Kg m-2)	0.25	0.13	0 – 4.37
Rain Columnar Content (Kg m-2)	0.30	0.67	1 - 29.95
Graupel Columnar Content (Kg m-2)	0.07	0.28	0 – 40.15
Pristine Ice Columnar Content (Kg m-2)	0.62	1.87	0 – 18.01
Snow Columnar Content (Kg m-2)	0.34	0.40	0 – 4.80
Aggregate Columnar Content (Kg m-2)	0.04	0.02	0 – 4.66
Surface Rain Rate (mm hr-1)	0.97	10.85	1 – 184.69

In Figure 5.1, it is worth to noticing that almost all are around the peak value of 0 kg/m².

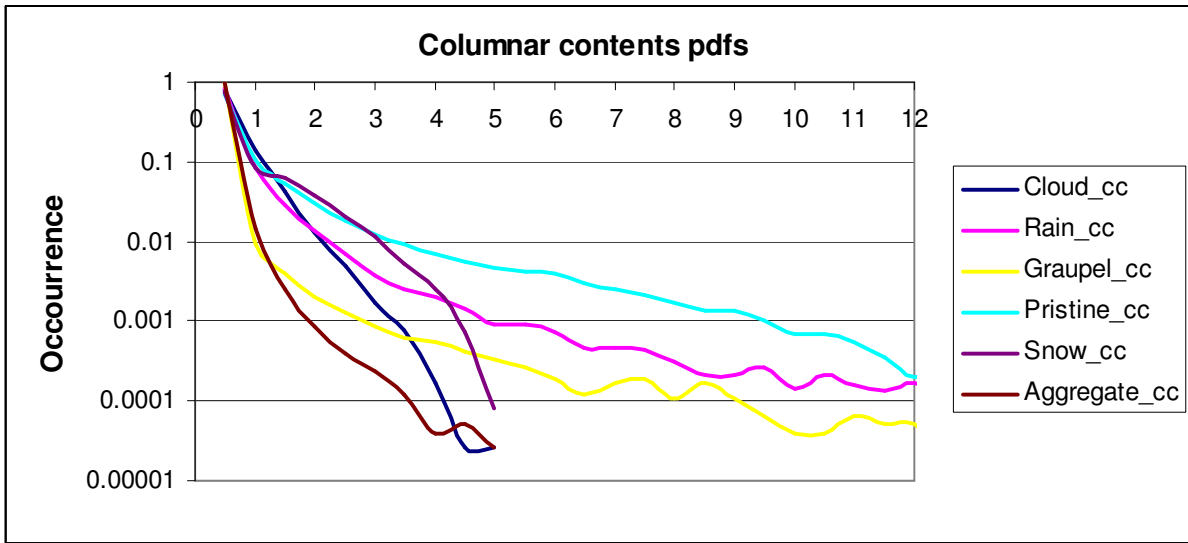


Figure 5.1. Probability Distribution Functions (PDFs) of the columnar contents (CC) of liquid and frozen hydrometeors within the CRD Turkish database.

Coupled with Table 5.2 it is obvious in Figure 5.2 that liquid precipitation have occasionally very high rates.

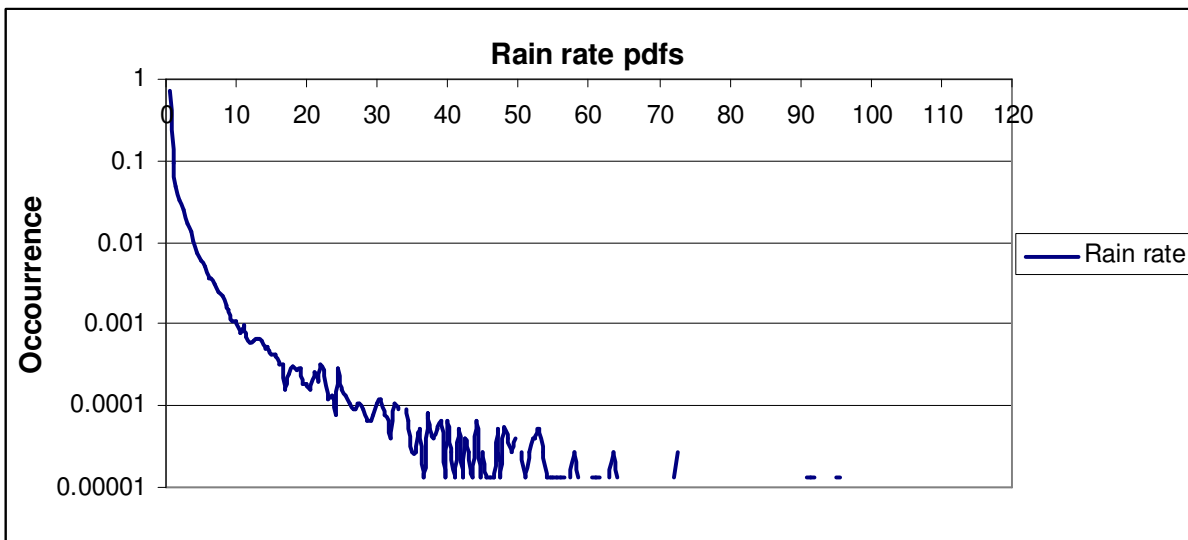


Figure 5.2. PDFs of liquid precipitation rates at the surface within the CRD Turkish database.

5.1.2. Upwelling Brightness Temperatures

Tables 5.3, 5.4 and 5.5 and Figures 5.3 to 5.5 provide the same statistics for the simulated upwelling TBs for all relevant SSM/I – SSMIS channels within the CRD database. Again, large variations may be observed, which are due to the wide range of different meteorological and environmental conditions of the simulated events.

Table 5.3. Statistics indexes of simulated TBs over land.

Over Land	Polarization	Mean	Variance	Spread	Mode
TB 19.35GHz	V	273.77	48.99	226.41 - 292.82	274.60
TB 19.35GHz	H	271.11	147.04	189.75 - 292.82	276.45
TB 22.235GHz	V	274.85	22.36	237.15 - 291.19	276.12
TB 37GHz	V	273.84	21.32	195.08 - 292.07	274.29
TB 37GHz	H	272.85	43.99	195.07 - 292.07	274.29
TB 85GHz	V	271.07	72.02	99.42 - 291.48	272.08
TB 85GHz	H	270.85	74.59	99.41 - 291.48	275.28
TB 91.66GHz	V	271.03	78.62	98.78 - 291.57	273.02
TB 91.66GHz	H	270.82	80.89	98.78 - 291.57	273.51
TB 150GHz	V	269.09	126.47	93.26 - 287.91	271.24
TB 150GHz	H	269.02	126.67	93.26 - 287.91	272.72
TB 183.31±7	H	262.93	67.97	94.12 - 278.73	264.23
TB 183.31±3	H	254.80	33.73	96.81 - 269.99	251.61
TB 183.31±1	H	243.50	20.41	110.96 - 259.34	239.63
TB 50.3GHz	H	268.99	21.21	155.88 - 285.25	268.62
TB 52.8GHz	H	258.14	7.55	174.75 - 269.66	258.35
TB 53.596GHz	H	244.13	3.97	190.95 - 252.56	244.35

Table 5.4. Statistics indexes of simulated TBs over ocean.

Over Ocean	Polarization	Mean	Variance	Spread	Mode
TB 19.35GHz	V	208.65	181.99	182.57 - 264.07	199.27
TB 19.35GHz	H	156.52	575.36	107.53 - 257.43	130.62
TB 22.235GHz	V	231.01	143.48	199.38 - 270.92	227.58
TB 37GHz	V	227.88	122.89	164.96 - 263.24	219.62
TB 37GHz	H	182.92	595.75	134.29 - 257.54	155.14
TB 85GHz	V	258.14	193.96	61.22 - 279.07	261.01
TB 85GHz	H	239.28	330.94	61.22 - 273.21	235.06
TB 91.66GHz	V	259.60	214.89	61.15 - 280.95	263.47
TB 91.66GHz	H	242.44	318.68	61.15 - 273.66	234.39
TB 150GHz	V	265.15	371.46	69.23 - 285.82	270.59
TB 150GHz	H	261.73	341.08	69.23 - 283.93	267.94
TB 183.31±7	H	260.26	259.16	75.08 - 277.95	263.17
TB 183.31±3	H	253.14	145.28	79.42 - 271.85	255.99
TB 183.31±1	H	242.71	67.05	91.12 - 261.73	239.46
TB 50.3GHz	H	240.2272	107.6749	122.17 - 265.50	238.52
TB 52.8GHz	H	254.4357	29.1565	140.14 - 265.20	255.59
TB 53.596GHz	H	243.3057	10.6125	167.20 - 251.35	243.33

Table 5.5. Statistics indexes of simulated TBs over coast.

Over Coast	Polarization	Mean	Variance	Spread	Mode
TB 19.35GHz	V	244.44	269.98	189.23 - 284.55	231.97
TB 19.35GHz	H	219.03	219.03	120.64 - 283.27	226.80
TB 22.235GHz	V	255.66	141.07	208.79 - 284.21	256.29
TB 37GHz	V	253.67	175.77	182.44 - 284.42	257.88
TB 37GHz	H	233.18	681.41	148.08 - 284.23	236.98
TB 85GHz	V	265.21	164.13	79.43 - 290.07	271.21
TB 85GHz	H	257.28	281.12	79.43 - 289.78	256.74
TB 91.66GHz	V	265.75	175.91	77.90 - 290.35	271.50
TB 91.66GHz	H	258.53	263.97	77.90 - 290.07	262.41
TB 150GHz	V	266.48	278.92	77.63 - 287.09	275.11
TB 150GHz	H	265.07	267.44	77.63 - 287.06	274.32
TB 183.31±7	H	260.86	175.08	81.28 - 277.00	264.79
TB 183.31±3	H	253.36	86.68	85.12 - 269.91	251.36
TB 183.31±1	H	242.63	38.25	96.25 - 259.23	239.44
TB 50.3GHz	H	256.25	116.79	142.92 - 281.46	257.05
TB 52.8GHz	H	256.19	17.40	160.36 - 267.91	256.67
TB 53.596GHz	H	243.47	6.00	183.74 - 251.99	243.46

A first glance on Figure 5.3 indicates first of all that there is a large difference between the PDF peaks for land and ocean, and it may be as a result of “cold” emission from the sea surface, which is coupled by land surfaces. Additionally, for each frequency there appears a large difference over ocean between the two polarizations, and it may be due to the higher ocean emissivity at vertical polarization.

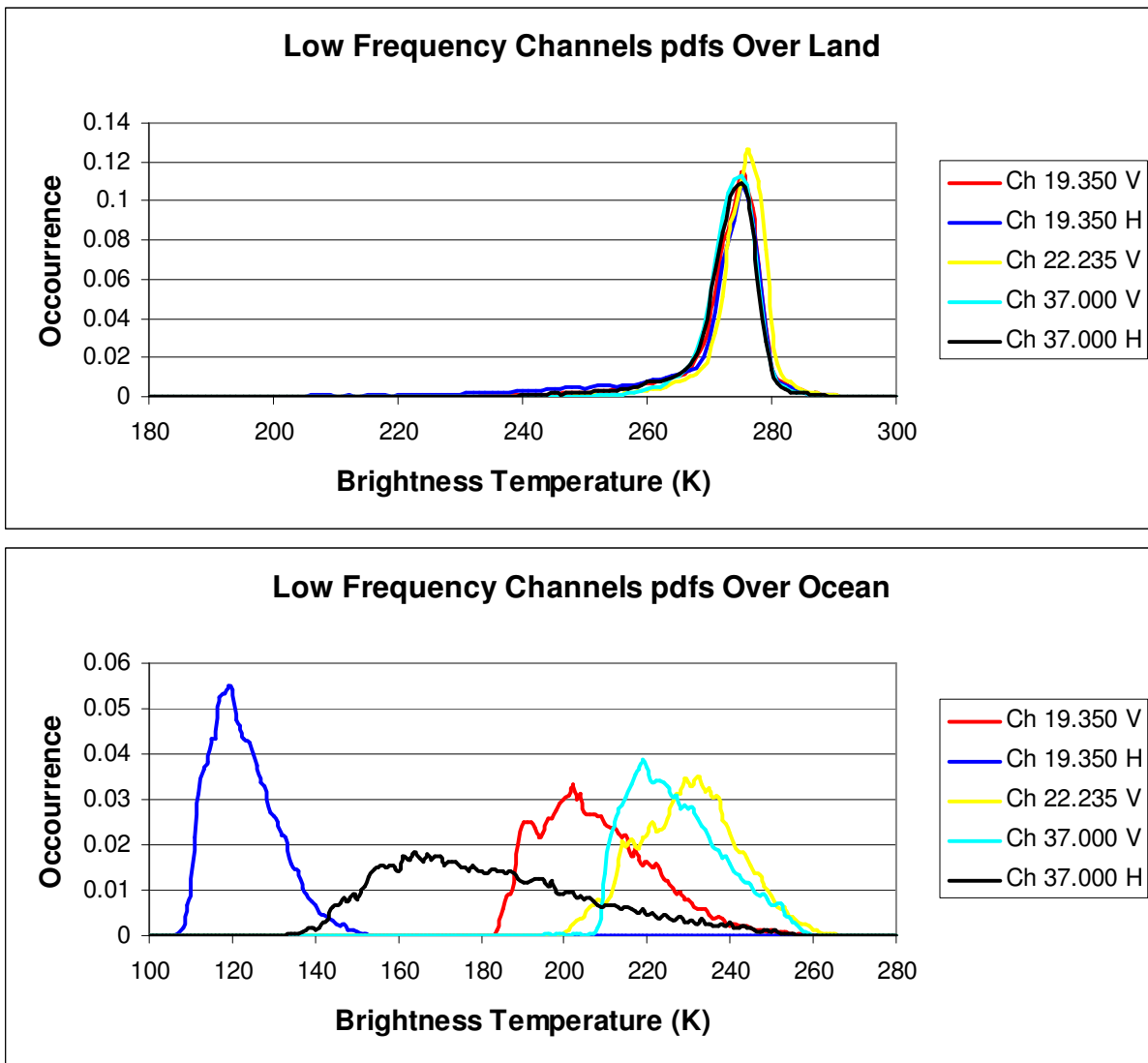


Figure 5.3. PDFs of the simulated upwelling TBs in the CRD / CDRD European database for the five low-frequency SSM/I – SSMIS window channels over land (top) and ocean (bottom).

The graphs in Figure 5.4 indicate the differences between land and ocean as well as the two polarizations, which are comparatively lower than for the low-frequency channels. This is as a result of much larger atmospheric contribution to the upwelling TBs.

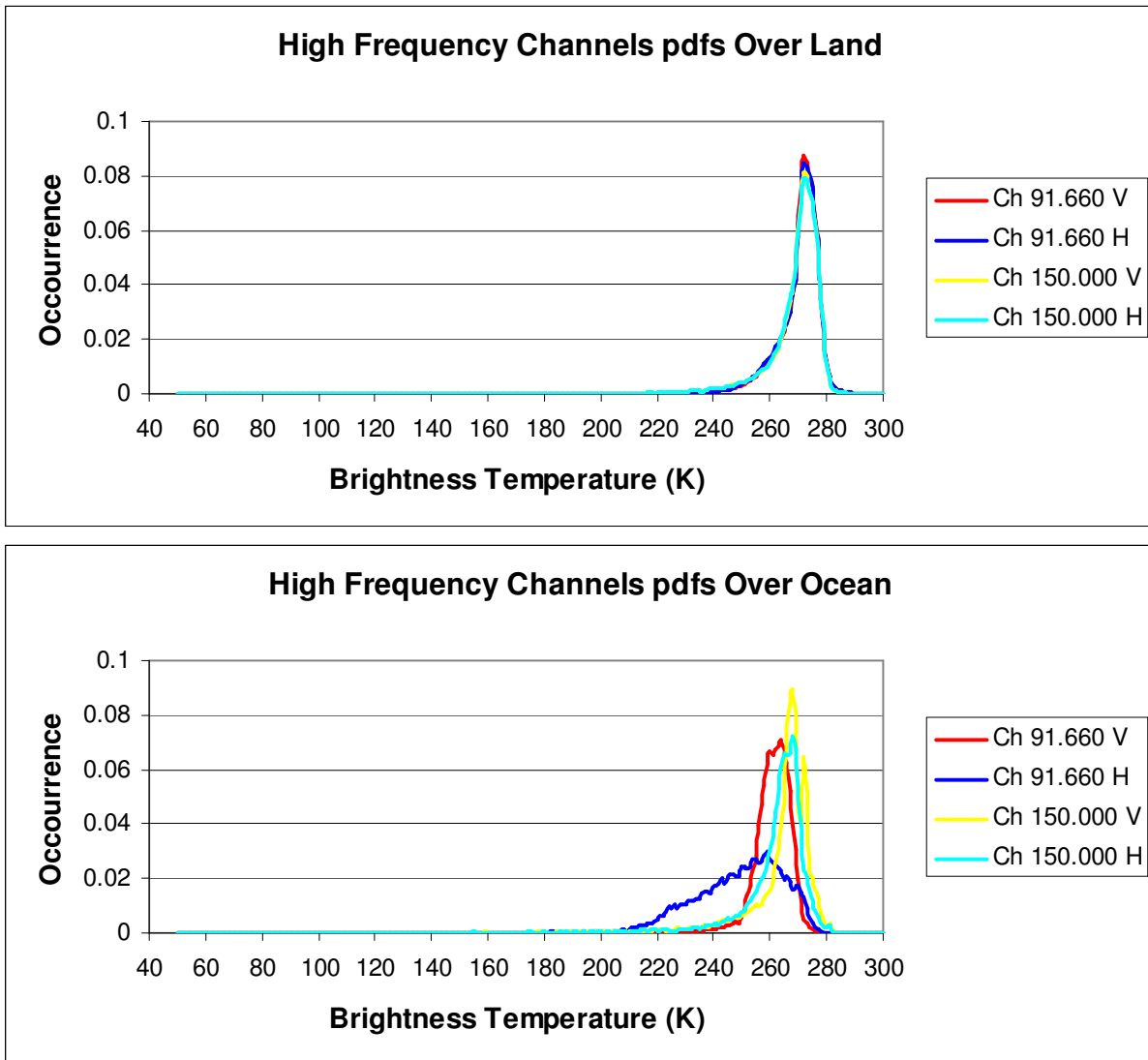


Figure 5.4. PDFs of the simulated upwelling TBs in the CRD / CDRD European database for the five high-frequency SSM/I – SSMIS window channels over land (top) and ocean (bottom).

In Figure 5.5 there are two cases with corresponding results for the other backgrounds that are not shown herein. In the upper figure as a result of absorption frequencies there is much effective role in the atmosphere than the back-ground. The probability distribution function (PDF) peak position in each panel is colder for channels with a peak weighting function at high atmospheric levels, whereas in the lower figure there is a cold tail for the 183.31 ± 7 channel. This is due to more external situation to the absorption band because it is influenced more from ice scatter.

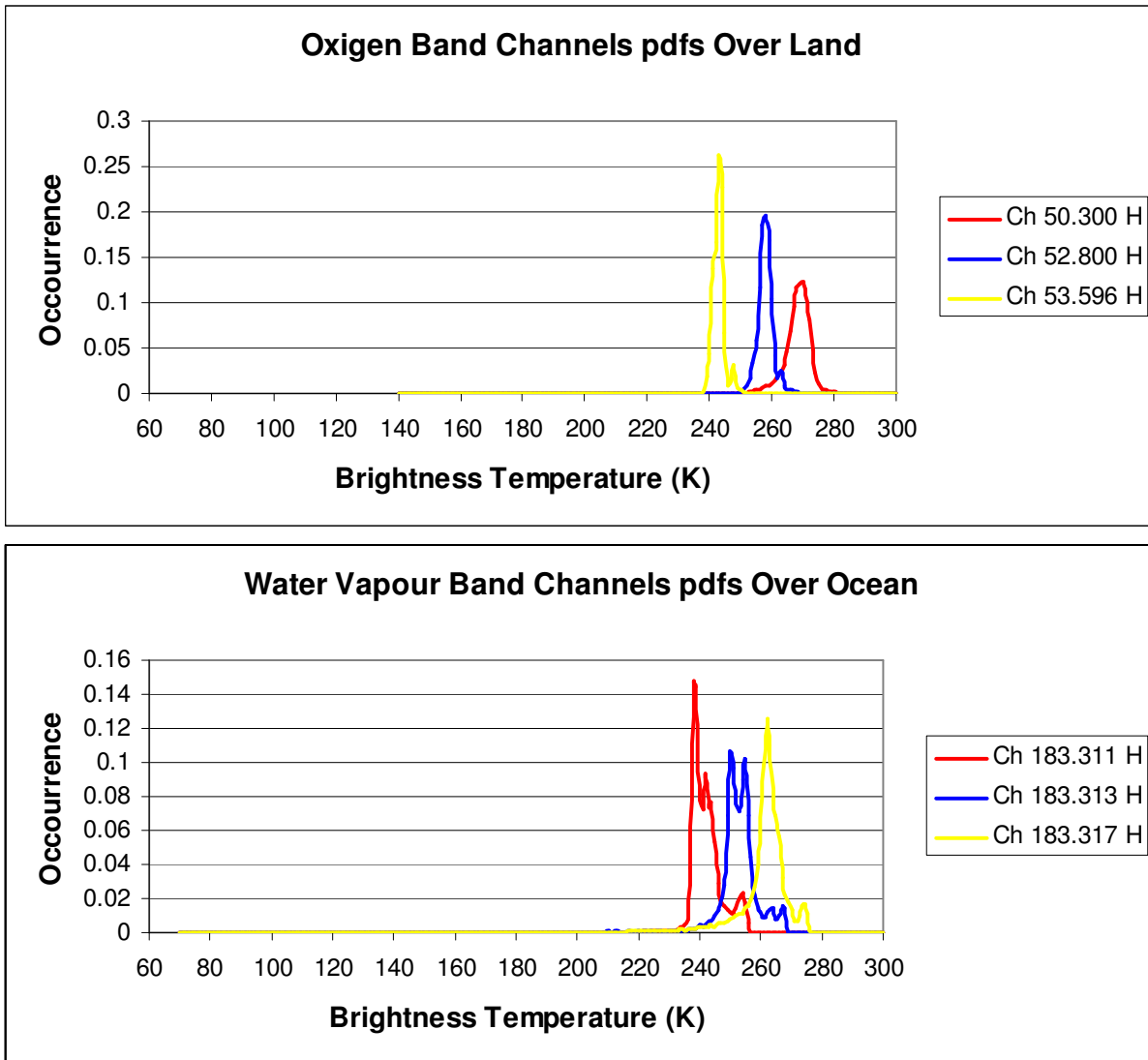


Figure 5.5. PDFs of the simulated TBs for the three lower SSMIS channels in the 50-60 GHz oxygen band over land (top) and for the three SSMIS channels in the 183 GHz water vapor line over ocean (bottom).

5.1.3. Comparison of Measured and Simulated Brightness Temperatures

In this figure (Figure 5.6), different colors are employed for the indication of the density concerning two databases around each 19-37 GHz “point”. They are in terms of the log-occurrences at all 19-37 GHz couples as shown in the color bar. The simulations database are more consistent with the measurements apart from the long tail in the simulations (especially at 19 GHz).

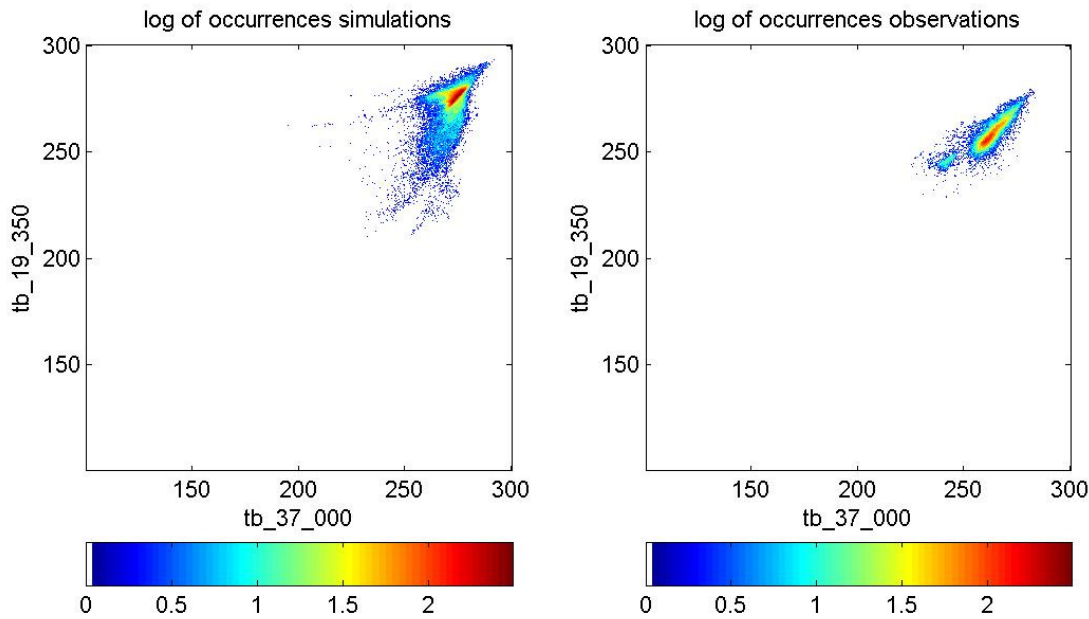


Figure 5.6. 19.35 GHz vs. 37 GHz scatterplot of the simulated TBs in the Turkish CRD database (top left) and of the measured TBs in the SSM/I – SSMIS measurements database (top right) – in both case, over land only.

Figure 5.7 represents in a better way than previous case as for the consistency of the simulations with the measurements. However, in Figure 5.6, 50.3 GHz is less sensitive to surface characteristics than the lower window frequencies.

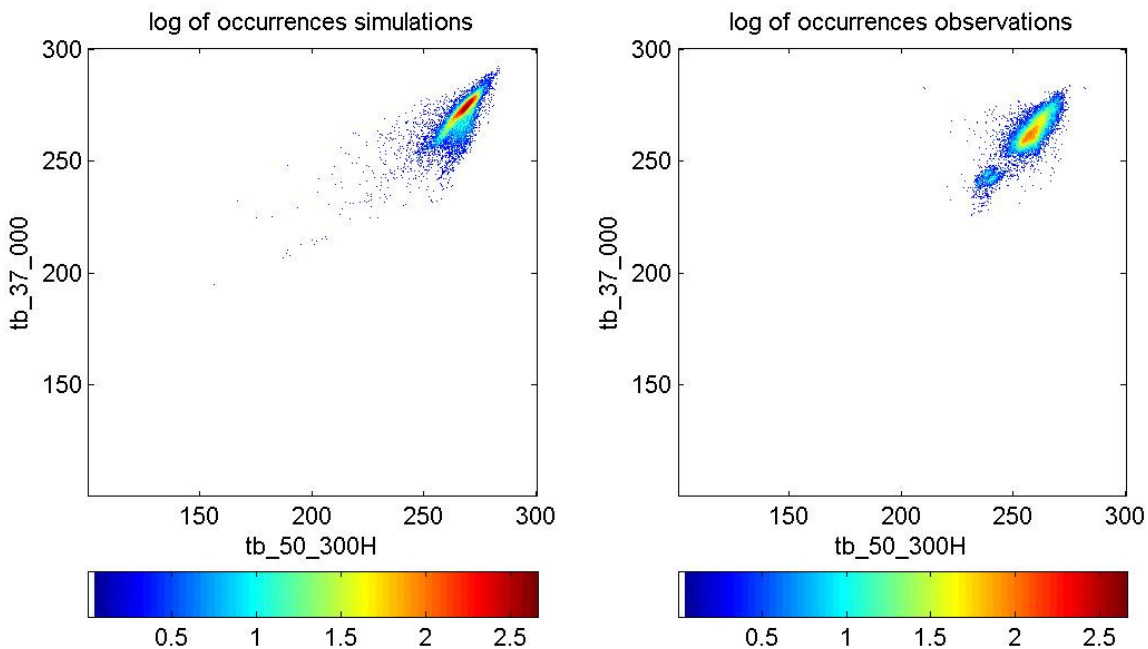


Figure 5.7. 37 GHz vs. 50.3 GHz scatterplot of SSMIS simulated and measured TBs.

Surface emissivity does not impact significantly on the upwelling TBs at these high window frequencies. However, exceptions are only in thin cloud presence with very low precipitation. On the other hand, the overall consistency for simulations database shows the ice contents that are simulated rather properly by the UW-NMS model, where an appropriate ice scattering parameterizations is considered.

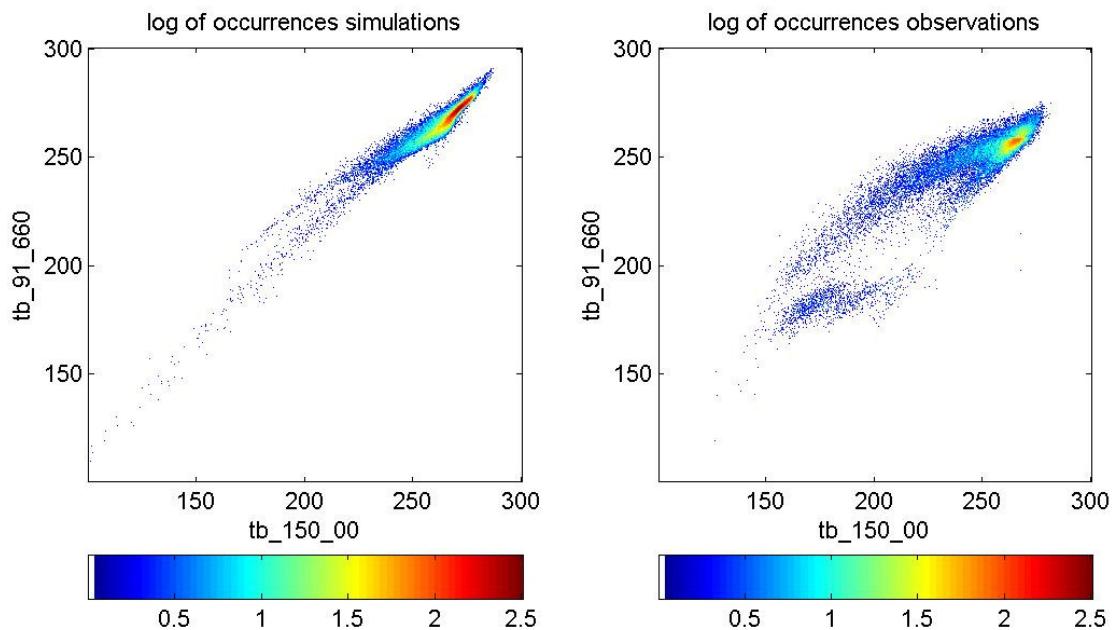


Figure 5.8. 91.66 GHz vs. 150 GHz scatterplot of SSMIS simulated and measured TBs.

Figure 5.9 presents intense water vapor line absorption frequencies at 183.31 GHz. Herein, the surface emissivity impact is negligible, but overall simulation consistency shows the ice contents, which are simulated by the UW-NMS model. Accordingly, appropriate ice scattering parameterizations are adopted especially at higher cloud portions.

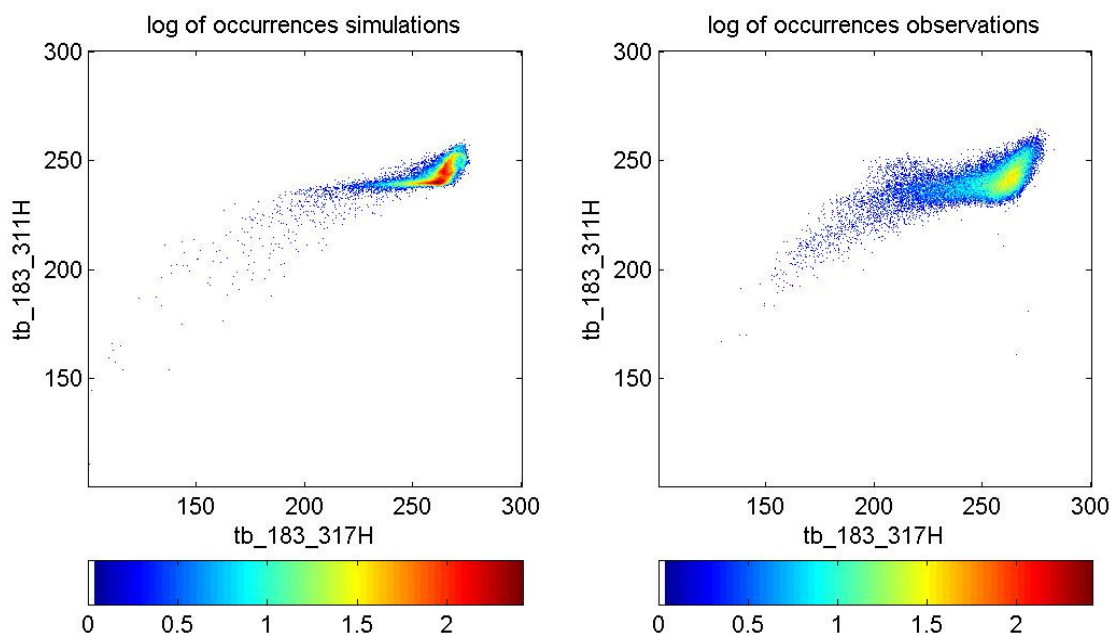


Figure 5.9. 183.31±3 GHz vs. 183.31±7 GHz scatterplot of SSMIS simulated and measured TBs.

5.2. Applications of the CDRD Algorithm

5.2.1. Comparisons of Radar and Retrieval

In Figure 5.12a, scatter diagrams are obtained by considerations of 1x1 and 3x3 resolution rain rate retrivals versus radar values, respectively. According to 45 degree line, the overall regression line indicates overestimation results with a very significant variability

deviations in Figure 5.12a. This is tantamount to saying that there are undeterminism, and therefore, one cannot depict the proper relationship between the two variables. In fact, there are many points that are zero for retrieval values given a set of radar results. On the other hand, in Figure 12b, 3x3 spatial filtering is applied to available data, and consequently, a better situation appears, but still the retrivals have overestimations for early data points.

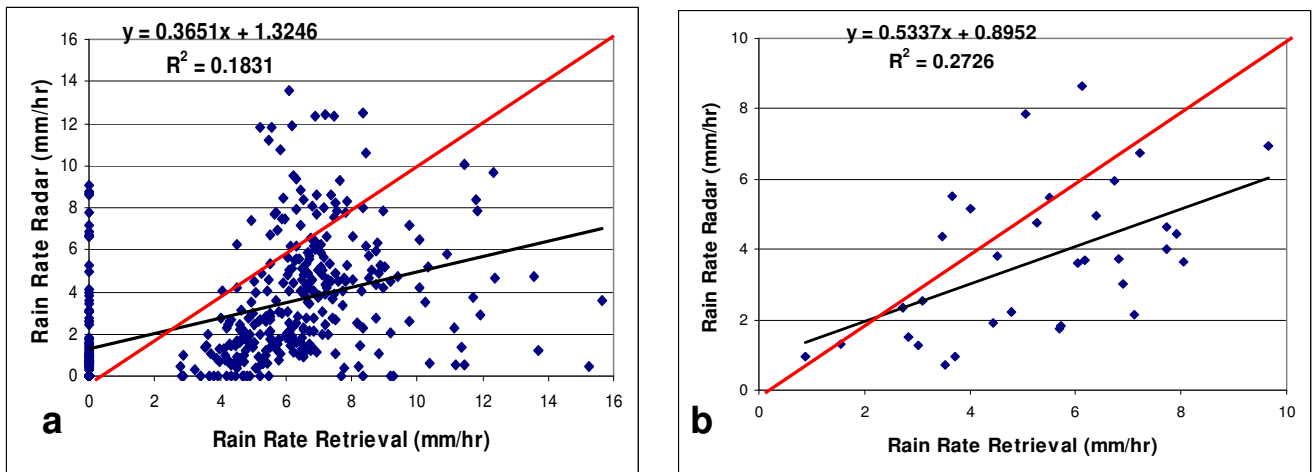


Figure 5.12. Scatter diagrams between radar and retrieval on 8 February 2009 at 05:41 GMT (a) original comparison, (b) after applying a 3X3 filter

The following table (Table 5.6) provide the statistical values corresponding to scatter diagrams in Figure 5.12 with both filtering situations. Comparison of the statistics for both cases in the last two columns of the table shows naturally that the wider the filter area the lower and more persistent are the parameters.

Table 5.6. Statistical features (8 February 2009 at 05:41 GMT)

Error Statistics	1X1 filter	3X3 filter
Mean Error	1.68	1.56
Mean absolute error	2.94	2.13
Mean squared error	14.64	6.41
Root mean square error	3.83	2.53
Standard deviation	3.44	2.02
Correlation coefficient	0.43	0.52
(Multiplicative) bias	1.55	1.42
URD-RMSE	14.18	1.61

So far as the rainfall occurrences are concerned, the following table (Table 5.7) includes different criteria that are already explained earlier during this project. It is obvious that the rainfall occurrences are more pronounced in the case of 3x3 filtering case than the finer resolution.

Table 5.7. Rainfall occurrence indices (8 February 2009 at 05:41 GMT)

Categorical Statistics	1X1 filter	3X3 filter
POD	0.82	1.00
BIAS	0.87	1.00
FAR	0.06	0.00
CSI	0.77	1.00
HR	0.80	1.00
POFD	0.26	-999

All what have been said about the two filtering cases are reflected in Figure 5.13 in the form of spatial patches of rainfall occurrences and their quantities as shown in the color bars. It is obvious that the occurrence patterns are almost the same, but as for the rainfall amounts are concerned, there are discrepancies. For instance, in the retrieval case (Figure 5.13.a) although there are several sub-regions (peaks) with comparatively high rainfall amounts, radar case (Figure 5.13.b) has only a single peak.

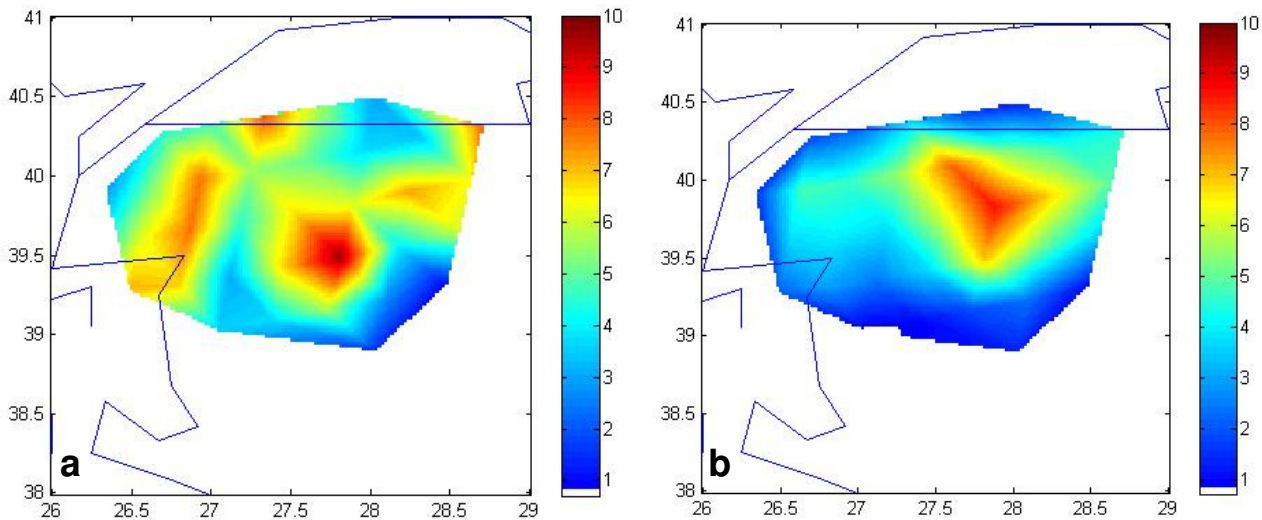


Figure 5.13. Patterns by using 3X3 filter on 8 February 2009 at 05:41 GMT (a) retrieval, (b) radar

Figure 5.14 is valid for 3 October 2008 at 05:44 GMT rainfall event both for retrieval and radar calculations. It is again obvious in Figure 5.15.a that there is a great scatter on the basis of one-cell resolution and similarly overestimation still prevails, but compared with the case in Figure 5.13 the scatter are not very much concentrated on a certain portion on the Cartesian coordinate system. Comparison between the two cases indicate that 3 October 2008 at 05:44 GMT event has less data points. On the other hand, coarser resolution (3x3 spatial filtering) yields better representation but still overestimation shows itself.

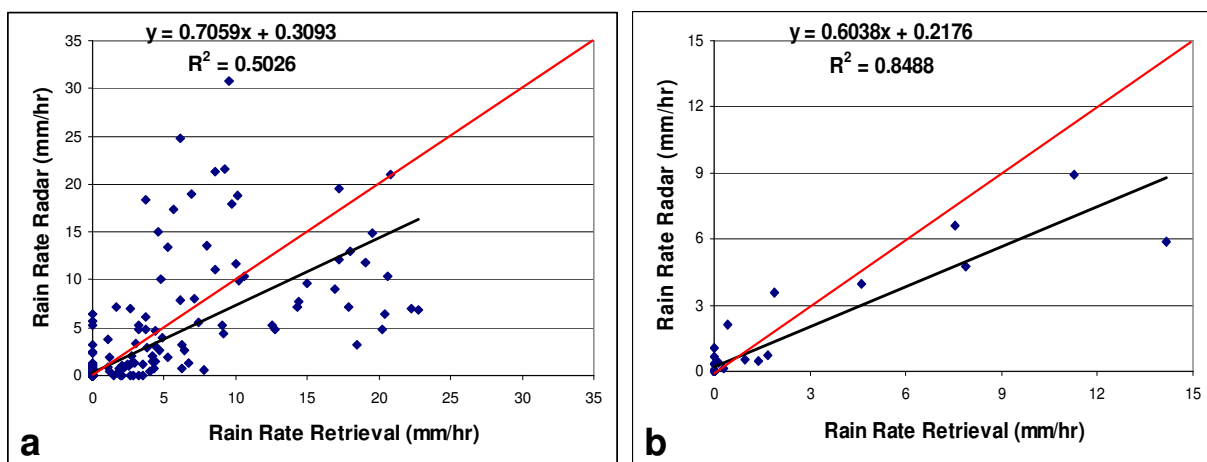


Figure 5.14. Scatter diagrams between radar and retrieval on 3 October 2008 at 05:44 GMT (a) original comparison, (b) after applying a 3X3 filter.

The statistical properties of both resolution cases, namely, 1x1 and 3x3 spatial averages are available in Table 5.8. Comparison of these statistics with the correspondings in Table 5.6 indicates that 3 October 2008 at 05:44 GMT event has more stable behaviour.

Table 5.8. Statistical features (3 October 2008 at 05:44 GMT)

Error Statistics	1X1 filter	3X3 filter
Mean Error	0.07	0.26
Mean absolute error	0.92	0.56
Mean squared error	8.40	2.20
Root mean square error	2.89	1.48
Standard deviation	2.90	1.48
Correlation coefficient	0.71	0.92
(Multiplicative) bias	1.06	1.28
URD-RMSE	4.85	0.95

According to table 5.9 unfortunately rainfall occurrence cannot be even confirmed with very high certainty in the case of 3 October 2008 at 05:44 GMT event than the previous one.

Table 5.9. Rainfall occurrence indices (3 October 2008 at 05:44 GMT)

Categorical Statistics	1X1 filter	3X3 filter
POD	0.75	0.72
BIAS	0.82	0.72
FAR	0.08	0.00
CSI	0.70	0.72
HR	0.94	0.88
POFD	0.02	0.00

The rainfall spatial pattern in Figure 5.15 has a better match between retrieval and radar data especially in the form of two patches. Hence, areal coverage-wise, they are similar. Additionally, in the lower patch the rainfall amounts are also verbally correspond with each other as low (high) rainfall points and in the retrieval pattern are in accordance with low (high) radar patterns. However, numerically they are different especially at high rainfall areas.

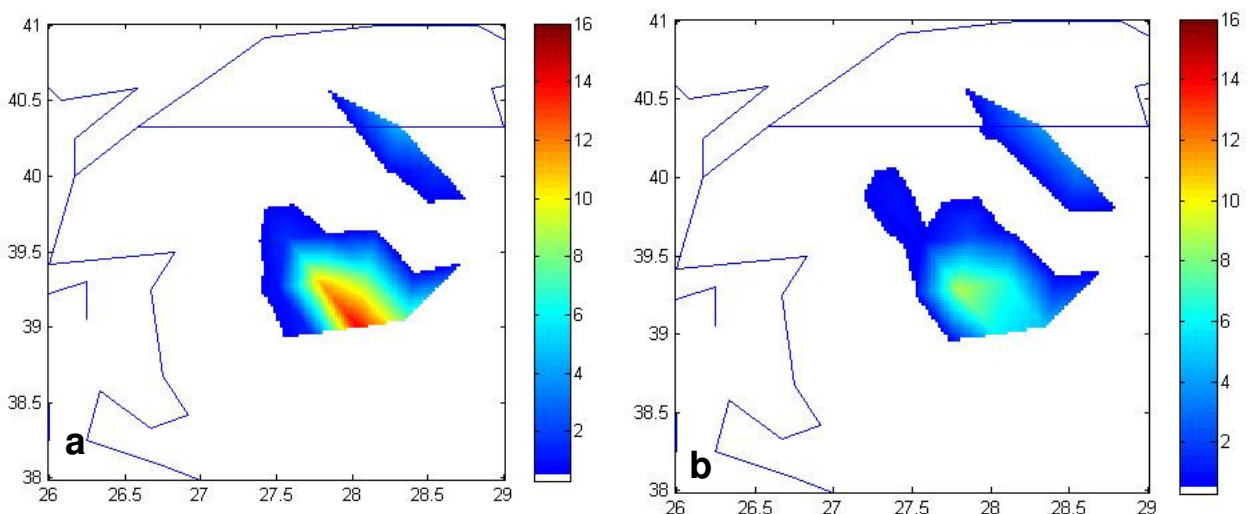


Figure 5.15. Patterns by using 3X3 filter on 3 October 2008 at 05:44 GMT (a) retrieval, (b) radar

A third case study example is shown in Figure 5.16 concerning the radar and retrieval (model estimation data scatter diagrams correspondingly for 21 March 2008 at 18:07 GMT. Both one-cell and 3-cell averaging (filtering) schemes have almost the same scatter on both Cartesian coordinate systems. In fact, it is very clear in Figure 5.16b that there is a non-linear relationship between the two sets of values. This is tantamount to saying that the proposed model cannot depict the variation feature between the retrieval and radar measurements.

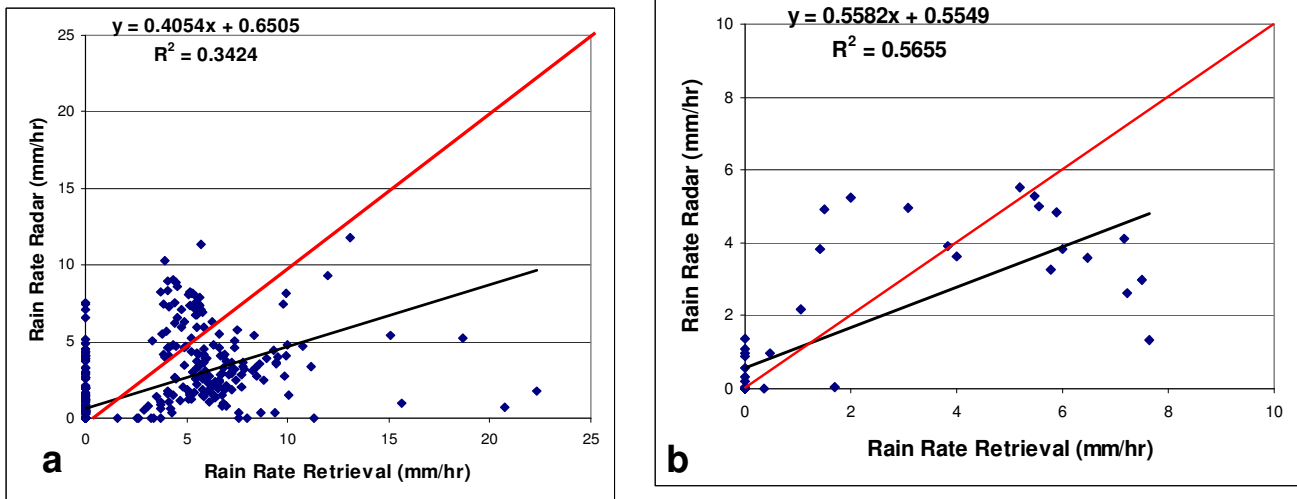


Figure 5.16. Scatter diagrams between radar and retrieval on 21 March 2008 at 18:07 GMT (a) original comparison, (b) after applying a 3X3 filter.

Table 5.10 is for the statistical quantities and Table 5.11 is for categorical statistics. Both statistical quantities and categorical statistics are good.

Table 5.10. Statistical features (21 March 2008 at 18:07 GMT)

Statistics	1X1 filter	3X3 filter
Mean Error	0.51	0.23
Mean absolute error	1.42	0.97
Mean squared error	7.68	3.05
Root mean square error	2.77	1.75
Standard deviation	2.73	1.75
Correlation coefficient	0.59	0.75
(Multiplicative) bias	1.35	1.15
URD-RMSE	13.63	59.24

Table 5.11. Rainfall occurrence indices (21 March 2008 at 18:07 GMT)

Categorical Statistics	1X1 filter	3X3 filter
POD	0.67	0.71
BIAS	0.70	0.75
FAR	0.05	0.05
CSI	0.64	0.69
HR	0.84	0.82
POFD	0.03	0.04

As the last example from rather mountainous area, Figure 5.17 depicts the spatial pattern on coarse and fine resolutions and again although they have similar areal coverage, the rainfall amounts are not so close. After the comparison of all the three previous cases it is possible to state that the current model adjustment for any one of these cases may yield far better results, but then it will yield not so good results for other cases. Perhaps, what may be suggested is that the retrieval model approach should be developed in such a manner to reduce the overall error from all the cases, this is tantamount to saying that the sum of the squares of the errors must be minimized.

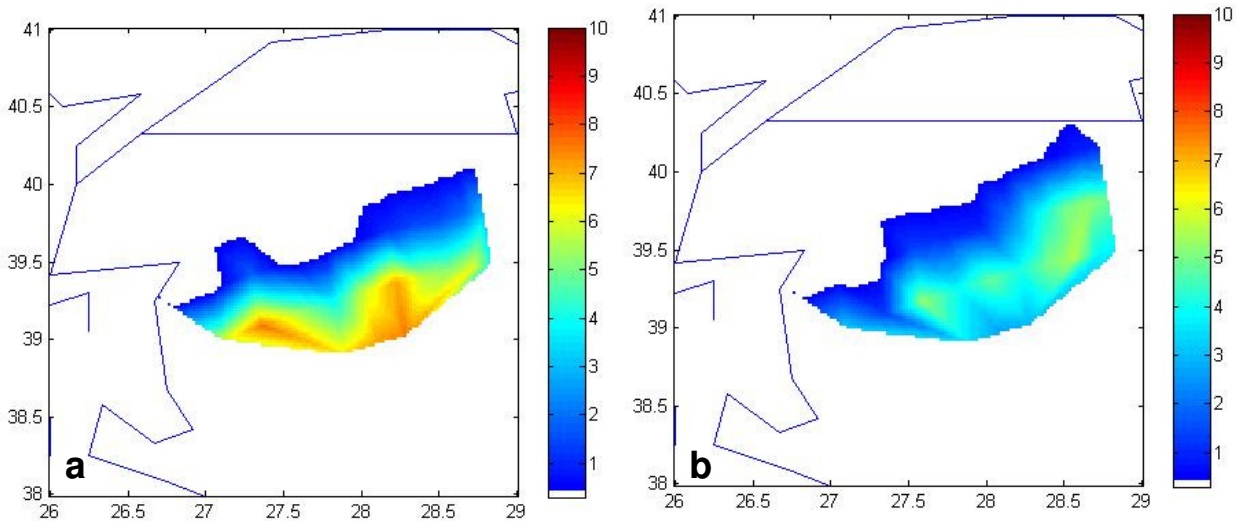


Figure 5.17. Patterns by using 3X3 filter on 21 March 2008 at 18:07 GMT (a) retrieval, (b) radar

9 September 2009 at 03:40 GMT case yields scatter diagrams as in Figure 5.18 and it has rather similar case to Figure 5.16, in the sense that the regression relationship is very close to linear and not as in Figure 5.17 non-linear.

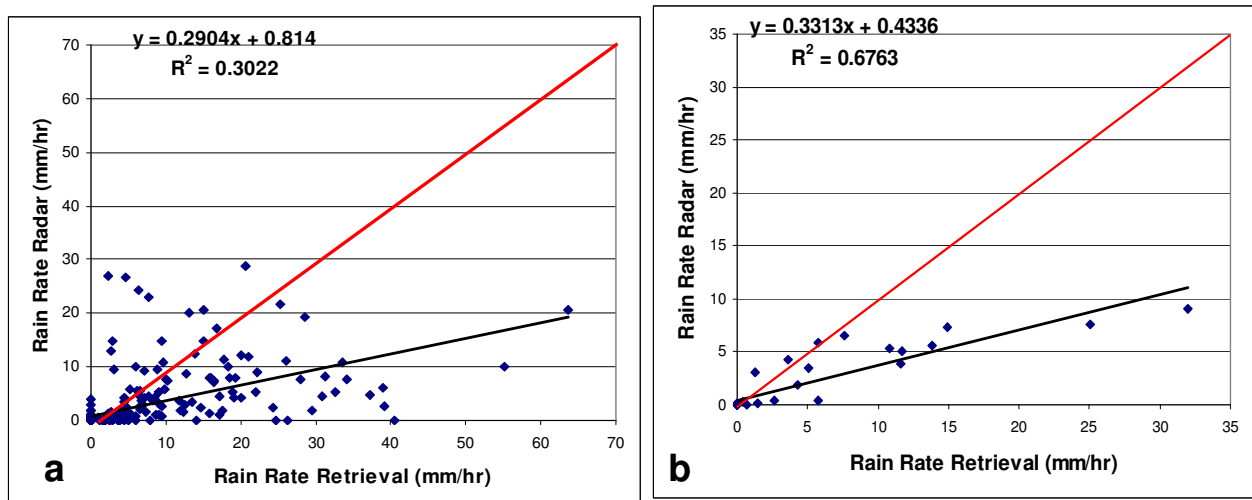


Figure 5.18. Scatter diagrams between radar and retrieval on 9 September 2009 at 03:40 GMT (a) original comparison, (b) after applying a 3X3 filter

Table 5.12 is for the statistical quantities and Table 5.13 is for categorical statistics. Both statistical quantities and categorical statistics are very good.

Table 5.12. Statistical features (9 September 2009 at 03:40 GMT)

Statistics	1X1 filter	3X3 filter
Mean Error	2.51	3.15
Mean absolute error	3.44	3.34
Mean squared error	63.49	40.57
Root mean square error	7.97	6.37
Standard deviation	7.57	5.64
Correlation coefficient	0.55	0.87
(Multiplicative) bias	2.15	2.25
URD-RMSE	15.78	21.08

Table 5.13. Rainfall occurrence indices (9 September 2009 at 03:40 GMT)

Categorical Statistics	1X1 filter	3X3 filter
POD	0.86	0.90
BIAS	0.99	0.90
FAR	0.13	0.00
CSI	0.77	0.90
HR	0.89	0.93
POFD	0.08	0.00

All the three previous rainfall events are from rather mountainous area, and therefore, the scatters cannot be accounted on the basis of atmospheric phenomena only, but also surface features in the form of morphology must also be considered. In order to check whether there is an effect of rugged area compared to rather flat surfaces, in Figure 5.19 comparatively flat area of İstanbul and its vicinity is adopted with the retrieval as well as radar patterns, separately. It is very interesting after the comparison of this figure with all three figures (Figures 5.16, 5.17 and 5.18) to depict that the retrieval and radar patterns have almost the same regional shape and also the quantitative rainfall values are rather close to each other.

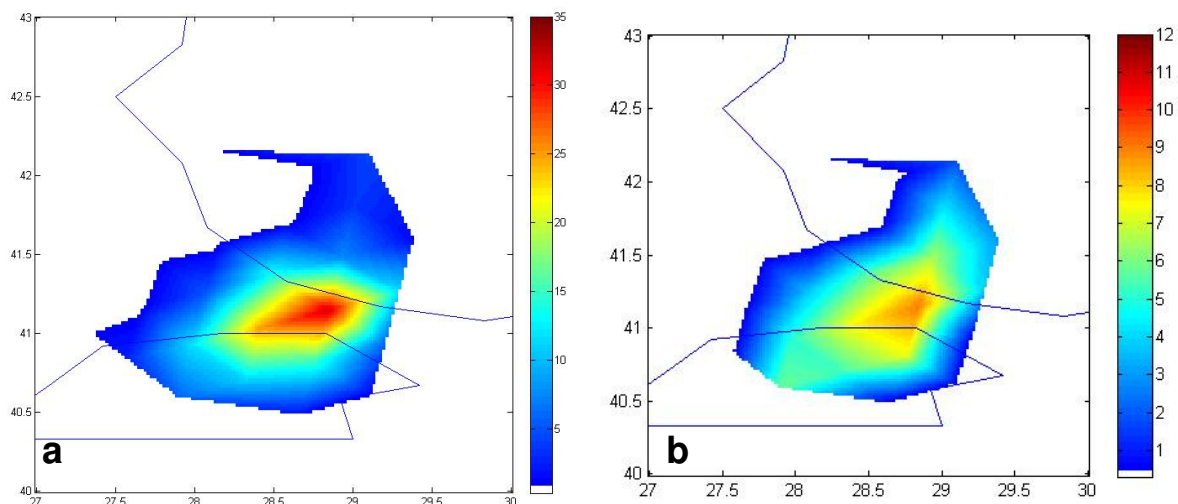


Figure 5.19. Patterns by using 3X3 filter on 9 September 2009 at 03:40 GMT (a) retrieval, (b) radar

5.2.2. Validation of Retrieval by using Raingauge

In this work H01 based on SSMI/S and H02 based on AMSU are used for validation by using raingauge. Turkish CDR database and Bayesian Algorithm for H01 and NEXRAD version of AMSU algorithm are used. All statistics are given in Tables 5.6 and 5.7. Moreover, common validation methodology in HSAF is applied to this research for validation.

Table 5.6. Summary results of PR-OBS-1 validation in Turkey over inner land

H01	Turkey	Land	Validation period: 1 st July 2008 - 30 June 2009 - Threshold rain / no rain: 0.25 mm/h										
Gauge	Class	Jul	Aug	Sep	Oct	Nov	Dec	Jan	Feb	Mar	Apr	May	Jun
Number of comparisons (ground obs.)	> 10 mm/h	0	12	196	17	45	0	12	0	0	1	0	44
	1-10 mm/h	1671	744	13426	5370	8119	7499	15882	18603	7626	9459	7527	4717
	< 1 mm/h	3246	1232	25065	15474	21879	32645	36493	46103	35365	28461	21365	10435
ME (mm/h)	> 10 mm/h	-	-10.66	-13.04	-12.60	-10.83	-	-2.66	-	-	-10.13	-	-5.76
	1-10 mm/h	-0.97	-4.27	-0.48	-0.71	-0.66	-0.33	-0.21	-0.18	-0.11	1.19	1.97	0.99
	< 1 mm/h	-0.14	0.24	0.16	0.11	-0.17	-0.06	-0.01	-0.01	-0.01	0.36	1.22	1.01
SD (mm/h)	> 10 mm/h	-	0.38	5.59	2.86	3.41	-	16.61	-	-	-	-	9.10
	1-10 mm/h	3.38	2.60	4.12	3.48	3.59	3.29	4.31	3.23	3.79	5.18	6.44	6.53
	< 1 mm/h	1.56	2.98	2.42	2.18	1.46	1.88	2.03	1.94	1.88	2.56	4.58	4.26
RMSE (mm/h)	> 10 mm/h	-	10.67	14.18	12.91	11.35	-	16.12	-	-	10.13	-	10.69
	1-10 mm/h	3.51	5.00	4.14	3.55	3.65	3.31	4.31	3.24	3.80	5.32	6.74	6.61
	< 1 mm/h	1.57	2.99	2.42	2.19	1.47	1.89	2.03	1.94	1.88	2.58	4.74	4.38
RMSE (%)	> 10 mm/h	-	100	94	99	93	-	145	-	-	100	-	100
	1-10 mm/h	228	142	230	209	187	197	220	214	228	311	431	403
	< 1 mm/h	293	553	597	440	323	456	416	409	419	504	992	830
CC	> 10 mm/h	-	-	0.15	-0.18	-0.09	-	-0.12	-	-	-	-	-0.20
	1-10 mm/h	-0.02	-0.22	0.05	0.04	0.11	0.32	0.20	0.13	0.21	0.18	0.16	0.03
	< 1 mm/h	0.15	0.30	0.02	0.08	0.06	0.04	0.08	0.08	0.09	0.15	0.13	0.18
POD	≥ 0.25 mm/h	0.15	0.09	0.19	0.15	0.01	0.10	0.12	0.13	0.11	0.22	0.35	0.34
FAR	≥ 0.25 mm/h	0.83	0.93	0.53	0.69	0.68	0.84	0.83	0.71	0.83	0.51	0.56	0.63
CSI	≥ 0.25 mm/h	0.09	0.04	0.16	0.12	0.08	0.06	0.07	0.10	0.07	0.18	0.24	0.22

Table 5.7. Summary results of PR-OBS-2 validation in Turkey over inner land

H02	Turkey	Land	Validation period: 1 st July 2008 - 30 June 2009 - Threshold rain / no rain: 0.25 mm/h											
			Jul	Aug	Sep	Oct	Nov	Dec	Jan	Feb	Mar	Apr	May	Jun
Gauge	Class													
	Number of comparisons (ground obs.)	> 10 mm/h	0	0	3	-	5	0	0	1	0	18	-	9
		1-10 mm/h	452	352	2864	-	2472	1800	6126	6763	3395	3464	-	1620
< 1 mm/h		1052	581	6515	-	7470	7961	14274	18339	12536	9413	-	3147	
ME (mm/h)	> 10 mm/h	-	-	-12.65	-	-10.39	-	-	-12.39	-	-12.40	-	-3.22	
	1-10 mm/h	3.20	13.47	-0.81	-	-1.63	-1.27	-1.38	-1.46	-1.28	-1.08	-	0.78	
	< 1 mm/h	2.29	3.19	0.22	-	-0.46	-0.44	-0.47	-0.46	-0.48	-0.33	-	1.38	
SD (mm/h)	> 10 mm/h	-	-	0.78	-	2.05	-	-	-	-	3.58	-	24.29	
	1-10 mm/h	17.64	30.55	4.20	-	1.35	0.77	1.26	0.83	1.04	1.85	-	9.04	
	< 1 mm/h	11.57	15.71	5.05	-	0.35	0.34	0.37	0.50	0.37	0.81	-	6.73	
RMSE (mm/h)	> 10 mm/h	-	-	12.67	-	10.55	-	-	12.39	-	12.87	-	23.13	
	1-10 mm/h	17.91	33.34	4.27	-	2.12	1.48	1.87	1.68	1.65	2.14	-	9.07	
	< 1 mm/h	11.79	16.02	5.05	-	0.58	0.56	0.60	0.68	0.60	0.88	-	6.87	
RMSE (%)	> 10 mm/h	-	-	100	-	94	-	-	100	-	89	-	166	
	1-10 mm/h	1094	2055	254	-	97	96	97	94	104	106	-	531	
	< 1 mm/h	2918	2406	1349	-	108	108	112	121	108	180	-	1642	
CC	> 10 mm/h	-	-	-	-	-0.23	-	-	-	-	0.03	-	-0.29	
	1-10 mm/h	0.23	0.11	0.03	-	0.30	0.16	0.36	0.21	0.16	0.26	-	0.00	
	< 1 mm/h	-0.02	0.24	-0.01	-	0.11	0.08	0.08	0.05	0.10	0.07	-	0.05	
POD	≥ 0.25 mm/h	0.11	0.21	0.13	-	0.08	0.06	0.10	0.09	0.06	0.14	-	0.21	
FAR	≥ 0.25 mm/h	0.55	0.61	0.43	-	0.23	0.33	0.37	0.26	0.36	0.31	-	0.64	
CSI	≥ 0.25 mm/h	0.10	0.15	0.12	-	0.08	0.06	0.09	0.09	0.05	0.14	-	0.15	

Values in Table 5.6 and Table 5.7 are presented in graphical form in Figure 5.20 and Figure 5.21, respectively. As for Figure 5.20 the following interpretation sequence can be drawn.

- 1) It is clear from Figure 5.20a that the standard deviation (SD) and root Mean square error (RMSE) have almost the same pattern, and therefore, in the future only RMSE must be considered.
- 2) RMSE variation for < 1 mm/h precipitation is comparatively smaller than the other alternative where the precipitation amounts lie within 1 mm/h and 10 mm/h interval. This is meaningful because extreme precipitation fluctuations are within this interval and also the number of precipitation occurrences in this interval is less than the occurrences, where precipitation is < 1mm/h.
- 3) The mean error (ME) values fluctuate around zero level for the case where precipitation is < 1mm/h, which indicates the suitability of the used model.
- 4) Unfortunately, the ME values for 1-10 mm/h interval have dominantly negatives, which means that the model yields biased results. However, since all the values fluctuate around almost -1.0 level it is possible to improve the model by introducing a constant value, which helps to shift -1.00 level to zero level.
- 5) In Figure 5.20b there are significant errors because precipitation category more than 10 mm/h includes very extreme values and accordingly their treatments must be dealt with a separate approach and model.

- 6) It is very obvious in Figure 5.20c that as the category values increase (from < 1 mm/h, to 1-10 mm/h, then to > 10 mm/h) so does the irregularity behaviour of the correlation coefficient. Although, there are not significant outlier appearance in < 1 mm/h correlation coefficient, for 1-10 mm/h the maximum correlation is in almost December
- 7) In Figure 5.20d FAR is usually high and CSI is very low.

Figure 5.21 graphs lead to the following sequence of interpretations.

- 1) In Figure 5.21a ME, SD and RMSE are parallel to each other. ME is negative for < 1.0 mm/hr and 1-10 mm/hr precipitation between November 2008 and April 2009. Other statistics are positive and low for this time interval. On the other hand, all statistic scores are high between July and September 2008 than others months.
- 2) Figure 5.21b includes very extreme case (> 10 mm/h) ME, SD and RMSE values, where again the ME has all negative values but all of them are around a horizontal line.
- 3) Figure 5.21c represents the correlation coefficient variation with time and as the category increases the correlation coefficient variation becomes more haphazard.
- 4) POD and CSI values are very low in Figure 5.21.d.

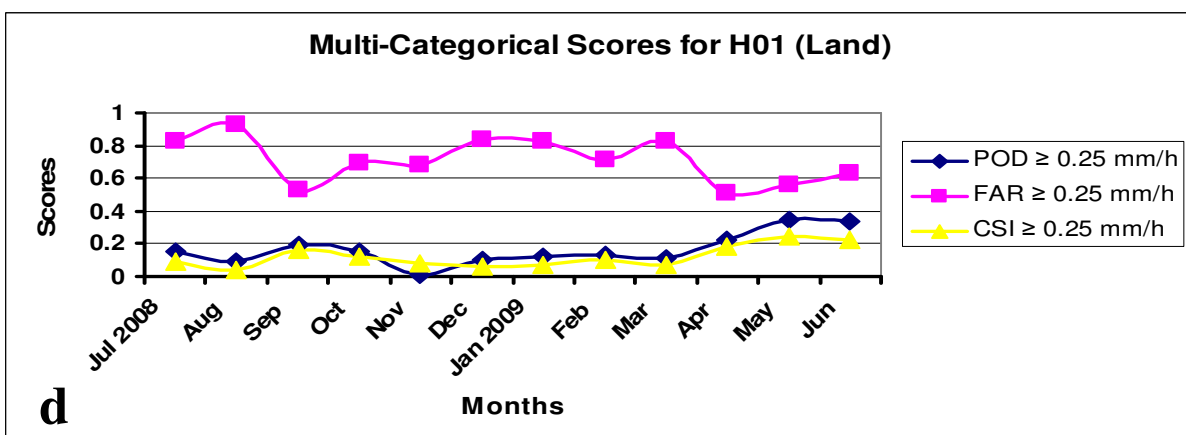
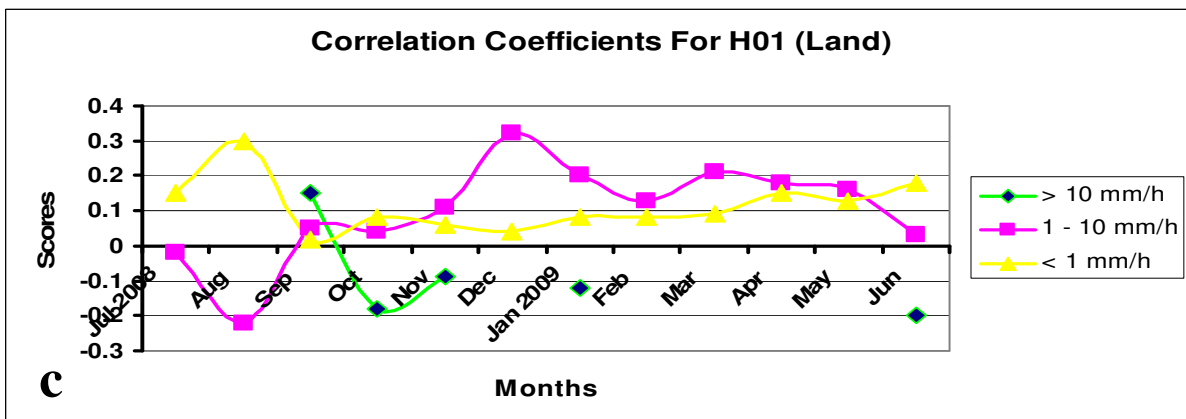
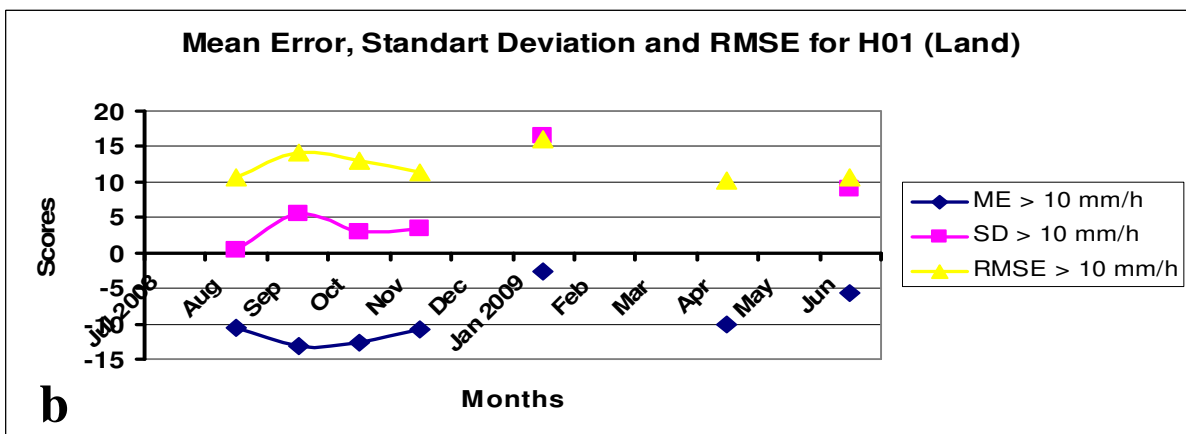
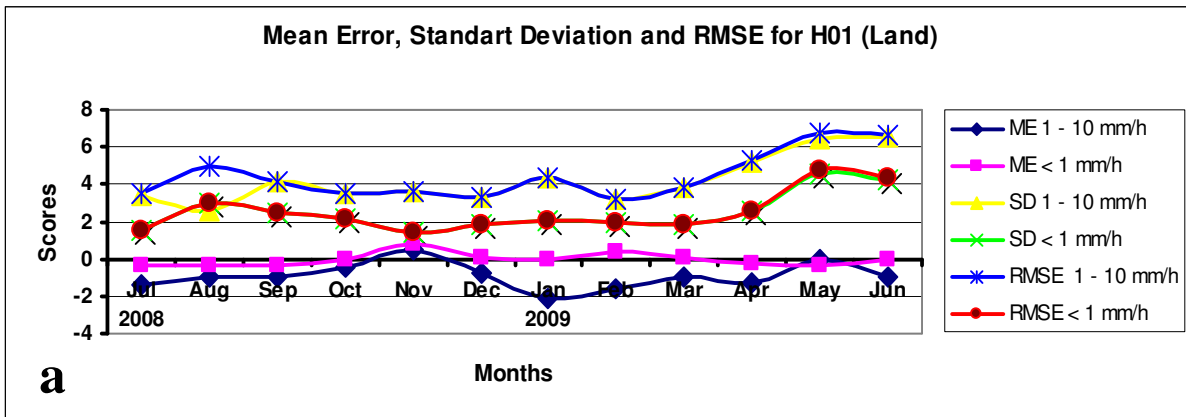


Figure 5.20. Continuous and multi-categorical statistics for inner land.

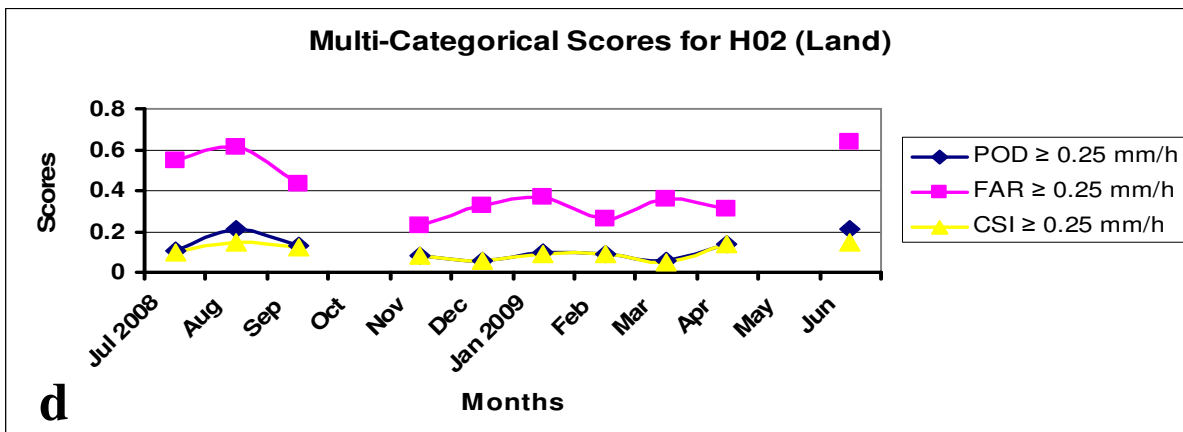
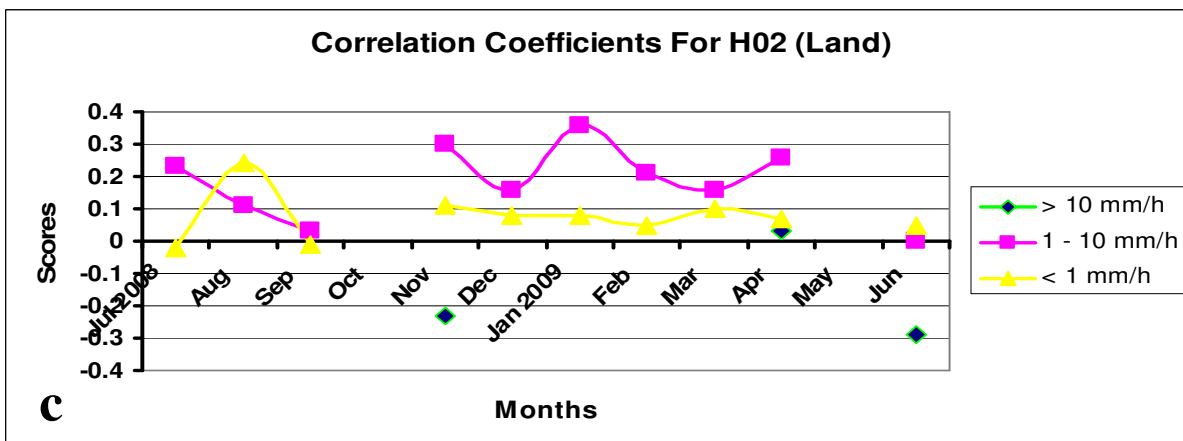
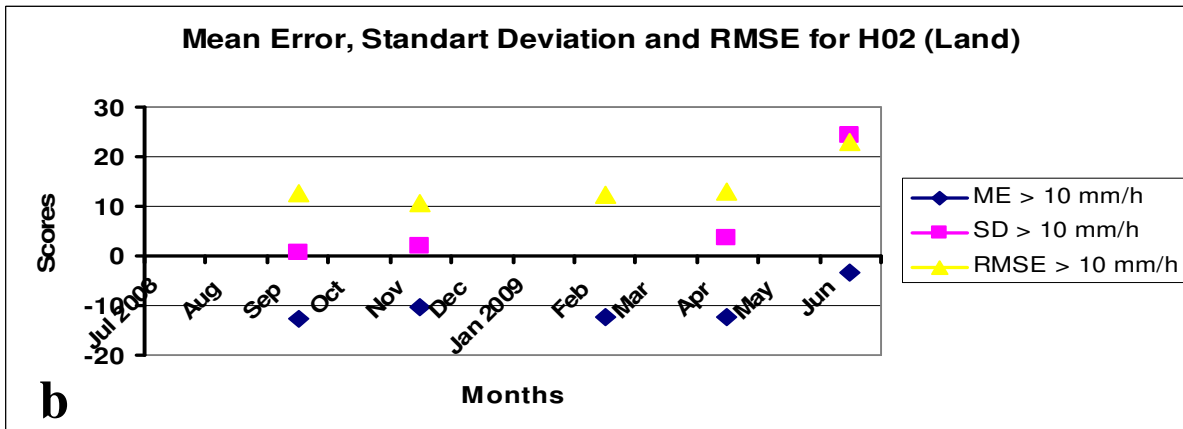
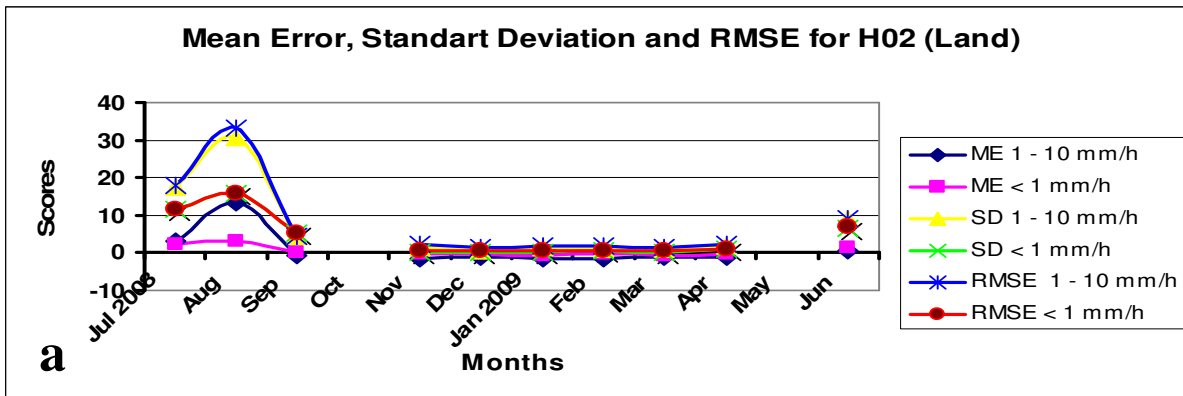


Figure 5.21. Continuous and multi-categorical statistics for inner land.

6. SUMMARY AND CONCLUSION

In this study, for PR-OBS-1 (Precipitation Rate at Ground by MW Conical Scanners) a Turkish database is structured and with these data the Bayesian approach is enhanced by all means. The rainfall products through such a study is validated by Turkish CDR on 206 rainfall stations within the same network and with 2 single polarization C band doppler radars. Additionally, NEXRAD version of PR-OBS-2 (Precipitation rate at ground by MW cross-track scanners) is also taken into consideration during the validation process.

As already defined earlier in this report four rainfall events in radar on 8 February 2009, 3 October 2008, 21 March 2008 and 9 September 2009 are compared with retrieval values and in all the cases overestimations are observed. Especially at the mountainous region of Balıkesir it is observed that coarser resolution (3x3 filter) indicates some improvements compared to finer filter cases. However, on 9 September 2009 rainfall event on comparatively flat area matches far better with the retrieval values and hence the spatial rainfall occurrence extent and numerical values are very close to each other than any other three cases in Balıkesir.

As a conclusion one can conclude that the retrieval yields overestimations. At this point due to the single polarization of radars lower values might be obtained also and this point must be taken into consideration in the future studies. Apart from all these, the coverage area of the radar will also help to improve the results, because in the mountainous areas there are blockage effects due to high hills.

PR-OBS-1 ve PR-OBS-2 products are rather low POD and CSI values compared with the validation results during July-August-2009 period, but FAR values are high.

Along with the results that emerge from this study it is advised to try and improve the efficiency of the algorithm in the future.

7. REFERENCES

- Bauer, P., L. Schanz and L. Roberti, 1998: Correction of the three-dimensional effects for passive microwave remote sensing of convective clouds. *J. Appl. Meteor.*, **37**, 1619-1632.
- Bohren, C.F., and D.R. Huffman, 1983: *Absorption and Scattering of Light by Small particles*. John Wiley & Sons, 530 pp.
- Cotton, W.R., G.J. Tripoli, R.M. Rauber and E.A. Mulvihill, 1986: Numerical simulation of the effects of varying ice crystal nucleation rate and aggregation processes on orographic snowfall. *J. Clim. Appl. Meteor.* **25**: 1658-1680.
- Czekala, H., P. Bauer, D. Jones, F. Marzano, A. Tassa, L. Roberti, S. English, J.P.V. Poiaraes Baptista, A. Mugnai and C. Simmer, 2000: Clouds and Precipitation. *Radiative Transfer Models for Microwave Radiometry* (C. Matzler, Ed.), COST Action 712, Directorate-General for Research, European Commission, Brussels, Belgium, 37-72.
- Di Michele S., A. Tassa, A. Mugnai, F.S. Marzano, P. Bauer and J.P.V. Poiaraes Baptista, 2005: The Bayesian Algorithm for Microwave-based Precipitation Retrieval: Description and application to TMI measurements over ocean. *IEEE Trans. Geosci. Remote Sens.*, **43**, 778-791.
- Di Michele S., F.S. Marzano, A. Mugnai, A. Tassa and J.P.V. Poiaraes Baptista, 2003: Physically-based statistical integration of TRMM microwave measurements for precipitation profiling. *Radio Sci.*, **38**, 8072-8088.
- English, S.J., and T.J. Hewison, 1998: A fast generic millimetre wave emissivity model. *Proc. SPIE on Microwave Remote Sensing of the Atmosphere and Environment*, 22- 30.
- Flatau P., G.J. Tripoli, J. Berlinde and W. Cotton, 1989: The CSU RAMS Cloud Microphysics Module: General Theory and Code Documentation. *Technical Report 451*, Colorado State University, 88 pp.
- Grenfell, T.C., and S.G. Warren, 1999: Representation of a nonspherical ice particle by a collection of independent spheres for scattering and absorption of radiation. *J. Geophys. Res.*, **104**, 31697-31709.
- Hewison, T.J., 2001: Airborne measurements of forest and agricultural land surface emissivity at millimeter wavelengths. *IEEE Trans. Geosci. Remote Sens.*, **39**, 393-400.
- Hewison, T.J., and S.J. English, 1999: Airborne retrievals of snow and ice surface emissivity at millimetre wavelengths. *IEEE Trans. Geosci. Remote Sens.*, **37**, 1871-1879.
- Hewison, T.J., and S.J. English, 2000: Fast models for land surface emissivity. *Radiative Transfer Models for Microwave Radiometry* (C. Matzler, Ed.), COST Action 712, Directorate-General for Research, European Commission, Brussels, Belgium, 117-127.
- Liu, G., C. Simmer and E. Ruprecht, 1996: Three-dimensional radiative transfer effects of clouds in the microwave spectral range. *J. Geophys. Res.*, **101**, 4289-4298.
- Mugnai, A., Casella, D., Formenton, M., Sanò, P., Tripoli, G. J., Leung, W. L., Smith, E. A., Mehta, A., 2009, *Generation of an European Cloud-Radiation Database to be used for PR-OBS-1 (Precipitation Rate at Ground by MW Conical Scanners)*, Activity Report, EUMETSAT – HSAF Project, 39 pp.
- Mugnai, A., S. Di Michele, F.S. Marzano and A. Tassa, 2001: Cloud-model based Bayesian techniques for precipitation profile retrieval from TRMM microwave sensors. *ECMWF/EuroTRMM Workshop on Assimilation of Clouds and Precipitation*, ECMWF, Reading, U.K., 323-345.
- Neshyba, S.P., T.C. Grenfell and S.G. Warren, 2003: Representation of a nonspherical ice particle by a collection of independent spheres for scattering and absorption of radiation: 2. Hexagonal columns and plates. *J. Geophys. Res.*, **108**, 4448-4465.

- Olson, W.S., P. Bauer, N.F. Viltard, D.E. Johnson, W.K. Tao, R. Meneghini and L. Liao, 2001: A melting layer model for passive/active microwave remote sensing applications. Part II: Simulation of TRMM observations. *J. Appl. Meteor.*, **40**, 1164-1179.
- Roberti, L., J. Haferman and C. Kummerow, 1994: Microwave radiative transfer through horizontally inhomogeneous precipitating clouds. *J. Geophys. Res.*, **99**, 707-716.
- Sanò, P., D. Casella, S. Dietrich, F. Di Paola, M. Formenton, W.-Y. Leung, A. Mehta, A. Mugnai, E.A. Smith and G.J. Tripoli, 2010: Bayesian estimation of precipitation from space using the Cloud Dynamics and Radiation Database (CDRD) approach: Application to case studies of FLASH and H-SAF Projects. *Nat. Hazards Earth Syst Sci.*, to be submitted.
- Schluessel, P.; and H. Luthardt, 1998: Surface wind speeds over the North Sea from Special Sensor Microwave/Imager observations. *J. Geophys. Res.*, **96**, 4845–4853.
- Surussavadee, C., 2006: Passive millimeter-wave retrieval of global precipitation utilizing satellites and a numerical weather prediction model. *Ph.D. dissertation*, Dept. Elect. Eng. and Comput. Sci., MIT, Cambridge, MA.
- Tassa, A., S. Di Michele, A. Mugnai, F.S. Marzano, P. Bauer and J.P.V. Poiaras Baptista, 2006: Modeling uncertainties for passive microwave precipitation retrieval: Evaluation of a case study. *IEEE Trans. Geosci Remote Sens.*, **44**, 78-89.
- Tassa, A., S. Di Michele, A. Mugnai, FS. Marzano and J.P.V. Poiaras Baptista, 2003: Cloud-model based Bayesian technique for precipitation profile retrieval from the Tropical Rainfall Measuring Mission Microwave Imager. *Radio Sci.*, **38**, 8074-8086.
- Tripoli G.J. and E.A. Smith, 2009: Scalable nonhydrostatic cloud/mesoscale model featuring variable-stepped topography coordinates: Formulation and performance on classic obstacle flow problems. *Mon. Wea. Rev.*, submitted.
- Tripoli, G.J., 1992: A nonhydrostatic model designed to simulate scale interaction. *Mon. Wea. Rev.*, **120**, 1342-1359.
- Tripoli, G.J., and W.R. Cotton, 1981: The use of ice-liquid water potential temperature as a thermodynamic variable in deep atmospheric models. *Mon. Wea. Rev.*, **109**, 1094-1102.
- Wiscombe, W.J., 1980: Improved Mie scattering algorithms. *Appl. Opt.*, **19**, 1505-1509.